Bridging Overlapping 2D Coarse and Fine Meshes Within the Phase Field Fracture Method

Zakaria Chafia, Julien Yvonnet, Jeremy Bleyer

▶ To cite this version:

Zakaria Chafia, Julien Yvonnet, Jeremy Bleyer. Bridging Overlapping 2D Coarse and Fine Meshes Within the Phase Field Fracture Method. International Journal for Numerical Methods in Engineering, 2025, 126 (9), ⟨10.1002/nme.70043⟩. ⟨hal-05059883⟩

HAL Id: hal-05059883

https://enpc.hal.science/hal-05059883v1

Submitted on 7 May 2025

International Journal for Numerical Methods in Engineering

WILEY

RESEARCH ARTICLE OPEN ACCESS

Bridging Overlapping 2D Coarse and Fine Meshes Within the Phase Field Fracture Method

Zakaria Chafia[1,2] | Julien Yvonnet[1] | Jérémy Bleyer[2]

[1]Université Gustave Eiffel, MSME, CNRS, UMR 8208, Marne-la-Vallée, France | [2]Ecole des Ponts ParisTech, NAVIER, CNRS, UMR 8205, Champs-sur-Marne, France

Correspondence: Julien Yvonnet (julien.yvonnet@univ-eiffel.fr)

Received: 3 April 2025 | **Revised:** 8 April 2025 | **Accepted:** 11 April 2025

Funding: This work was supported by Labex MMCD (ANR-11-LABX-022-01).

Keywords: Arlequin method | bridging domains | multiscale methods | phase field

ABSTRACT

A framework is proposed to bridge coarse and fine meshes in a single simulation within the phase field method for fracture. Fine meshes are used in the vicinity of localized defects to accurately capture crack initiation, while coarse meshes are used away from initial defects and include only crack propagation paths. This reduces the prohibitive computational times associated with uniformly fine meshes over the entire domain, or with the use of complex adaptive meshes in the phase field method. The coupling between the two overlapping meshes is achieved using a variational formulation in which the energies of the models associated with the fine and coarse meshes are weighted in the superposition zone. Two situations are considered. The first includes the resolution of the phase field problem only in the fine mesh, while the coarse mesh is limited to the undamaged elastic problem. In the second situation, cracks can propagate in both the fine and coarse mesh. Variational formulations and associated finite element implementations are detailed. Numerical examples are presented, showing the potential of this approach to significantly reduce computational costs in the phase field method for cracking without affecting the accuracy.

1 | Introduction

The phase field method, introduced in References [1, 2], is nowadays one of the most popular computational methods for simulating cracking processes. Its key advantages include the ability to handle crack initiation, propagation, coalescence, multiple cracks, and arbitrary geometric configurations. It is based on a variational formulation of the crack problem, in tandem with a regularized approach to limit the damage gradient, as well as a smooth description of discontinuities.

Several formulations can be found in the literature: Lancioni et al. [3], Amor et al. [4], Miehe et al. [5–8], Pham et al. [9], Ambati et al. [10], Borden et al. [11], Wu et al. [12], Nguyen et al. [13] (see also [14–21]).

The method has been extended for modeling anisotropic fracture in References [22–32], and applied to many problems, such as ductile fracture [33], dynamic fracture [34, 35], cohesive fracture [36, 37], hydraulic fracture [38], topology optimization for resistance to cracking [39], fracture in microtomography image-based models of microstructures [40–42], among many others.

The equations arising from the variational principle in the phase field imply at minimum two sets of equations, which need to be solved concurrently. For this purpose, two approaches are commonly used. On one hand, a robust algorithm using a staggered scheme has been introduced in Reference [6], which consists of solving decoupled problems. A damage problem is solved by fixing the displacement field, and a mechanical problem is solved

---

https://doi.org/10.1002/nme.70043

by fixing the damage variable. The main drawback of this scheme is that small loading steps are required to obtain converged solutions. On the other hand, the monolithic scheme consists of solving a coupled system of displacement and phase field equations simultaneously in a single step. This approach is efficient and allows larger loading increments, but is less robust, as it encounters convergence issues. Several attempts to improve monolithic solvers can be found in References [43–47]. A discussion of phase field problem solving can be found in Reference [48].

One issue in the phase field method is the need for a fine mesh along crack paths to capture the regularized description of the discontinuities. Typically, several elements covering the regularized crack width are required. Studies of large domains containing localized defects may then be limiting for the method, if the defect constrains the spatial discretization for the whole structure.

To overcome this limitation, several approaches have been developed in recent years. First, high-performance computing (HPC) can be used. The main idea is to divide the domain into several subdomains, on which computations are performed in parallel. In this context, different techniques can be found, such as MPI (Message Passing Interface) [49] for distributed-memory machines, OpenMP (Open Multi-Processing) [50] for shared-memory machines, and CUDA (Compute Unified Device Architecture) [51] for GPU acceleration. The computational efficiency and scalability for large-scale simulations are enhanced using two principal approaches. On the one hand, domain decomposition methods decompose the global problem into smaller, independent sub-problems, associated with each subdomain, which are solved concurrently. Classical techniques include the Schur methods [52, 53], the finite element tearing and interconnecting (FETI) method [54, 55], the balancing domain decomposition (BDD) method [56], Neumann–Neumann methods [57, 58] and Schwarz domain decomposition [59, 60] among others. On the other hand, in a collaborative approach, data partitioning methods involve dividing a large computational domain into smaller subdomains assigned to different computational cores, ensuring communication and data sharing as needed. To solve linear and non-linear problems within this approach, parallel direct solvers can be used, including UMFPACK [61], SuperLU [62], and MUMPS [63, 64]. The efficiency of this kind of solver may be limited for large-scale problems due to their computational costs and memory requirements. The disadvantage of direct solvers can be overcome by using iterative solvers [65–68] and an appropriate preconditioner [69–75] to accelerate their convergence rate. The application of parallel computing with the phase field method can be found in [76–80].

Another way to improve the computational efficiency within the phase field approach is to use adaptive mesh refinement algorithms [81–90]. These methods can significantly reduce computation time and memory storage. However, one of their drawbacks within the phase field method is the need for remeshing during crack propagation at each time step, which penalizes the efficiency.

Alternatively, global/local approaches can be used for modeling damage at reduced costs. One notable advancement in this context is the development of model bridging techniques such as the Arlequin method [91, 92] or the bridging domain method [93, 94], in which two models, possibly described with different kinematics and different discretizations, are bridged in a single simulation through an overlapping region and a variational approach. In Reference [95], a non-intrusive global/local method [96] has been adopted for the first time to simulate damage using the phase field method. This technique couples a global model representing the overall structure with a more detailed local model that captures localized damage processes. It has also been used in References [97–99] and has been extended to ductile fracture [100], hydraulic fracture [101] and anisotropic brittle fracture [30]. Other methods have been developed for reducing computational costs within the phase field approach, including the application of s-version finite element method for damage modeling [102], reduce order model-based fracture simulation [103, 104] and staggered scheme acceleration algorithm [105].

In the present work, an approach is developed to reduce computational costs of the phase field method when cracks nucleate from localized defects within a large structure, with different scale orders between the characteristic length of the defect and that of the structure. For this purpose, the framework of the Arlequin [91, 92] model bridging technique is adopted, where overlapping meshes are used. A fine mesh is adopted in regions of interest to model localized damage and accurately capture crack initiation, and a coarse-mesh is used elsewhere to reduce computational time. First, the method is developed for modeling the crack nucleation and propagation only in the fine mesh region, assuming that the coarse mesh region remains undamaged. Then, the method is extended to model the damage occurring in both fine and coarse regions. In this case, cracks initiate in the fine regions and can propagate through the coupling zones into the coarse region. The main novelty of this work is the development of the coupling framework between phase field models in both fine and coarse meshes, which has not been investigated so far, to our best knowledge. The phase field method is briefly reviewed in Section 2. The Arlequin framework is reviewed in Section 3. The application of the Arlequin framework for simulating damage employing the phase field method is presented in Section 4. Finally, numerical applications demonstrating the accuracy and efficiency of the proposed approach and its validation is provided in Section 5.

2 | The Phase Field Approach for Fracture Simulation

In this work, the phase field method for quasi-brittle fracture is briefly reviewed. Let us consider an open domain $\Omega \subset \mathbb{R}^D$ of dimension D and its boundary $\partial\Omega$ of dimension $D-1$. Let $\partial\Omega_u$ and $\partial\Omega_F$ be the parts of the boundary on which Dirichlet and Neumann boundary conditions are prescribed, respectively, such that $\partial\Omega = \partial\Omega_u \cup \partial\Omega_F$ and $\partial\Omega_u \cap \partial\Omega_F = \emptyset$. The total energy functional $\mathcal{E}(\boldsymbol{u}, d)$, according to [1], is given by:

$$\mathcal{E}(\boldsymbol{u}, d) = \int_{\Omega} \psi_e(\boldsymbol{\varepsilon}(\boldsymbol{u}), d)\, d\Omega + \int_{\Omega} \psi_f(d)\, d\Omega - \int_{\Omega} \boldsymbol{f}^* \cdot \boldsymbol{u}\, d\Omega - \int_{\partial\Omega_F} \boldsymbol{F}^* \cdot \boldsymbol{u}\, dS \tag{1}$$

where $\boldsymbol{u}$ is the displacement field, $\boldsymbol{\varepsilon}(\boldsymbol{u}) = \frac{1}{2}\left(\nabla(\boldsymbol{u}) + \nabla(\boldsymbol{u})^T\right)$ is the infinitesimal strain tensor and d is the damage variable. $\psi_e(\boldsymbol{u}, d)$ denotes the elastic energy density and $\psi_f(d)$ refers to the fracture energy density. $\boldsymbol{f}^*$ and $\boldsymbol{F}^*$ are body forces and prescribed forces on the boundary $\partial\Omega_F$, respectively.

The phase field framework developed in References [5, 7, 8] is considered. The elastic energy density, in this model, is split into positive and negative parts using the spectral decomposition of the strain tensor, which is given as:

$$\psi_e(\boldsymbol{\varepsilon}(\boldsymbol{u}), d) = (g(d))\psi_e^+(\boldsymbol{\varepsilon}(\boldsymbol{u})) + \psi_e^-(\boldsymbol{\varepsilon}(\boldsymbol{u})) \tag{2}$$

in which $g(d) = (1-d)^2$ is the degradation function applied only on the positive part of the elastic energy density, $\psi_e^+(\boldsymbol{\varepsilon}(\boldsymbol{u}))$ and $\psi_e^-(\boldsymbol{\varepsilon}(\boldsymbol{u}))$ refer to the positive and negative parts of the elastic energy density expressed as:

$$\psi_e^\pm(\boldsymbol{\varepsilon}(\boldsymbol{u})) = \frac{\lambda}{2}\left(\langle \mathrm{Tr}(\boldsymbol{\varepsilon})\rangle_\pm\right)^2 + \mu \mathrm{Tr}\left((\boldsymbol{\varepsilon}^\pm)^2\right) \tag{3}$$

where λ and μ are the Lamé's parameters, Tr(.) is the trace operator, $\boldsymbol{\varepsilon}^+$ and $\boldsymbol{\varepsilon}^-$ denote the positive and the negative parts of the strain tensors, respectively, which are expressed by:

$$\boldsymbol{\varepsilon}^\pm = \sum_{i=1}^{k} \langle \varepsilon^i \rangle_\pm \boldsymbol{n}^i \otimes \boldsymbol{n}^i, \quad k = 2,\ 3 \tag{4}$$

where $\langle x \rangle_\pm = \frac{1}{2}(x \pm |x|)$, ε^i and $\boldsymbol{n}^i$ are the eigenvalues and eigenvectors of the strain tensor $\boldsymbol{\varepsilon}$. The constitutive law is expressed (see, e.g., [8]) by:

$$\boldsymbol{\sigma} = \left((1-d)^2 + k\right)\left\{\lambda\langle Tr\boldsymbol{\varepsilon}\rangle_+ \boldsymbol{1} + 2\mu\boldsymbol{\varepsilon}^+\right\} + \lambda\langle Tr\boldsymbol{\varepsilon}\rangle_- \boldsymbol{1} + 2\mu\boldsymbol{\varepsilon}^- \tag{5}$$

where k is a small positive numerical parameter serving to avoid loss of stability in case of fully damaged elements.

In this work, the so-called AT2 model [8] is considered for the fracture energy density:

$$\psi_f(d) = \psi_c\left(d^2 + \ell_0^2 \nabla d \cdot \nabla d\right) \tag{6}$$

where $\nabla(\cdot)$ is the gradient operator, ℓ_0 is the characteristic length that governs the width of the damage zone, ψ_c is a specific fracture energy density, considered here to be a material property and which can be related to the critical stress σ_c and the fracture toughness G_c by:

$$\psi_c = \frac{\sigma_c^2}{2E} = \frac{G_c}{2\ell_0} \tag{7}$$

where E is the Young's modulus.

The functional in Equation (1) is not convex with respect to both unknowns $(\boldsymbol{u}, d)$, but is convex with respect to each variable separately [47]. To solve this minimization problem, a robust algorithm using a staggered scheme [8] is considered. Consequently, an incremental problem is obtained, where two coupled sets of equations are solved sequentially: A damage problem is solved by fixing the displacement field, and then a mechanical problem is solved by fixing the damage field d.

2.1 | Damage Problem

Given the displacement field u, the minimization of the total energy functional (1) with respect to the damage field is expressed as: Find $d \in \mathcal{D} = \left\{d \in H^1(\Omega) \mid 0 \le d \le 1 \quad \text{on} \quad \Omega\right\}$, such that $\forall \delta d \in \mathcal{D}^0 = H^1(\Omega)$,

$$\begin{aligned} D_{\delta d}\mathcal{E}(\boldsymbol{u}, d) = \int_\Omega & -2(1-d)\psi_e^+(\boldsymbol{\varepsilon}(\boldsymbol{u}))d\Omega \\ & + 2\psi_c\left(d + \ell_0^2 \nabla d \nabla(\delta d)\right)d\Omega = 0 \end{aligned} \tag{8}$$

where $D_{\delta d}\mathcal{E}(\boldsymbol{u}, d)$ is the directional derivative of $\mathcal{E}(\boldsymbol{u}, d)$ in the direction of δd. The associated Euler-Lagrange equations to Equation (8) are given by:

$$\begin{cases} (1-d)\psi_e^+ - \psi_c\left(d - \ell_0^2 \Delta d\right) = 0 & \text{in} \quad \Omega \\ \nabla d \cdot \boldsymbol{n} = 0 & \text{on} \quad \partial\Omega \end{cases} \tag{9}$$

where $\Delta(\cdot)$ is the Laplacian operator, $\boldsymbol{n}$ is the output normal vector on the boundary $\partial\Omega$.

The weak form of the damage problem is expressed as:

$$\int_\Omega (\psi_e^+ + \psi_c) d\delta d d\Omega + \psi_c \ell_0^2 \nabla d \nabla(\delta d) d\Omega = \int_\Omega \psi_e^+ \delta d d\Omega \tag{10}$$

To avoid non-physical self-healing phenomena of damage, an irreversibility condition is imposed on the phase field variable by an appropriate choice of the source term (the right-end term in Equation (10)). At every point in Ω, the damage variable is an increasing function of load evolution. Accordingly, a history functional is introduced in Reference [8] which is given as:

$$\mathcal{H} = \max_{\tau \in [0,t]}\left[\langle \psi_e^+(\varepsilon;\ \tau) - \psi_c \rangle_+\right] \tag{11}$$

where t is a pseudo time parameter describing the load evolution.

The weak form of Equation (10) can be written as shown in Equation (12):

$$\int_\Omega (\mathcal{H} + \psi_c) d\delta d d\Omega + \psi_c \ell_0^2 \nabla d \nabla(\delta d) d\Omega = \int_\Omega \mathcal{H} \delta d d\Omega \tag{12}$$

2.2 | Mechanical Problem

Given the damage field d, the minimization of the total energy functional (1) with respect to the displacement field is expressed as: Find $\boldsymbol{u} \in \mathcal{U} = \left\{\boldsymbol{u} \in H^1(\Omega) \mid \boldsymbol{u} = \boldsymbol{u}^* \quad \text{on} \quad \partial\Omega_u\right\}$ such that $\forall \delta\boldsymbol{u} \in \mathcal{U}^0 = \left\{\delta\boldsymbol{u} \in H^1(\Omega) \mid \delta\boldsymbol{u} = 0 \quad \text{on} \quad \partial\Omega_u\right\}$,

$$\begin{aligned} D_{\delta u}\mathcal{E}(\boldsymbol{u}, d) = \int_\Omega & \sigma(\boldsymbol{\varepsilon}(\boldsymbol{u}), d) : \boldsymbol{\varepsilon}(\delta\boldsymbol{u}) d\Omega - \int_\Omega \boldsymbol{f}^* \cdot \delta\boldsymbol{u} d\Omega \\ & - \int_{\partial\Omega_F} \boldsymbol{F}^* \cdot \delta\boldsymbol{u} dS = 0 \end{aligned} \tag{13}$$

The Euler-Lagrange equations associated to Equation (13) are given by:

$$\begin{cases} \nabla \cdot (\boldsymbol{\sigma}) + \boldsymbol{f}^* = 0 & \text{in} \quad \Omega \\ \boldsymbol{u} = \boldsymbol{u}^* & \text{on} \quad \partial\Omega_u \\ \boldsymbol{\sigma}\boldsymbol{n} = \boldsymbol{F}^* & \text{on} \quad \partial\Omega_F \end{cases} \tag{14}$$

where $\nabla \cdot (.)$ denote the divergence operator.

To avoid the nonlinearity related to the strain-tensor decomposition, two shifted strain tensor split algorithms were introduced in Reference [42] and expressed by:

$$\boldsymbol{\varepsilon}^{\pm}_{n+1} \simeq \mathcal{P}^{\pm}_{n} : \boldsymbol{\varepsilon}_{n+1} \tag{15}$$

in which

$$\mathcal{P}^{\pm} = \frac{\partial \boldsymbol{\varepsilon}^{\pm}}{\partial \boldsymbol{\varepsilon}} \tag{16}$$

where $\boldsymbol{\varepsilon}^{\pm}_{n+1}$ and $\boldsymbol{\varepsilon}_{n+1}$ are computed at load increment t_{n+1}. The computation of the projector tensors $\mathcal{P}^{\pm}_{n}$ are performed at the previous load increment t_n using the algorithm proposed in Reference [106].

This allows us to rewrite the stress/strain relationship in Equation (5) as follows:

$$\boldsymbol{\sigma}(\boldsymbol{\varepsilon}, d) = \mathcal{C}(d) : \boldsymbol{\varepsilon} \tag{17}$$

where

$$\begin{aligned} \mathcal{C}(d) = {} & \left((1-d)^2 + k\right)\left[\lambda \mathcal{R}^{+}[1][1]^T + 2\mu \mathcal{P}^{+}\right] \\ & + \lambda \mathcal{R}^{-}[1][1]^T + 2\mu \mathcal{P}^{-} \end{aligned} \tag{18}$$

in which $[1] = \{1; 1; 0\}^T$ and

$$\mathcal{R}^{+}(\boldsymbol{\varepsilon}) = \frac{1}{2}(sign(tr(\boldsymbol{\varepsilon})) + 1), \quad \mathcal{R}^{-}(\boldsymbol{\varepsilon}) = \frac{1}{2}(sign(-tr(\boldsymbol{\varepsilon})) + 1) \tag{19}$$

The weak form of the displacement problem is then expressed as:

$$\int_{\Omega} \boldsymbol{\varepsilon}(u) : \mathcal{C}(d) : \boldsymbol{\varepsilon}(\delta \mathbf{u}) d\Omega = \int_{\Omega} \boldsymbol{f}^{*} \cdot \delta u d\Omega + \int_{\partial \Omega_F} \boldsymbol{F}^{*} \cdot \delta u dS \tag{20}$$

For a detailed implementation of the phase field method, see, for example, [42].

3 | The Arlequin Method

The Arlequin method [91, 107] is a multiscale framework to solve problems in which two spatial scales co-exist. A computational domain Ω is decomposed into a coarse-scale domain and a fine-scale domain, which can overlap. The coupling between both domains, which can include different models, kinematics, or meshes with different sizes, is performed through a weak coupling. The main advantage of the Arlequin method is its ability to analyze phenomena at fine scales, for example, near defects, while considering regions near the defect by coarser models or meshes, and then to reduce drastically computational times as compared to using the fine model/mesh in the whole domain.

Let us consider an open domain $\Omega \subset \mathbb{R}^D$ and its boundary $\partial\Omega$ of dimension $D - 1$. Let us consider the overlapping subdomains Ω_1 and Ω_2 and their boundaries $\partial\Omega_1$ and $\partial\Omega_2$, respectively, such that $\Omega = \Omega_1 \cup \Omega_2$ and $\Omega_c = \Omega_1 \cap \Omega_2 \neq \emptyset$, where Ω_c represents the coupling zone (see Figure 1). Let $\partial\Omega^1_u$ and $\partial\Omega^1_F$ be the parts of the boundary $\partial\Omega_1$ on which Dirichlet and Neumann boundary conditions are prescribed, respectively, such that $\partial\Omega_1 = \partial\Omega^1_u \cup \partial\Omega^1_F$ and $\partial\Omega^1_u \cap \partial\Omega^1_F = \emptyset$. Let $\partial\Omega^2_u$ and $\partial\Omega^2_F$ be the parts of the boundary $\partial\Omega_2$ on which Dirichlet and Neumann boundary conditions are prescribed, respectively, such that $\partial\Omega_2 = \partial\Omega^2_u \cup \partial\Omega^2_F$ and $\partial\Omega^2_u \cap \partial\Omega^2_F = \emptyset$.

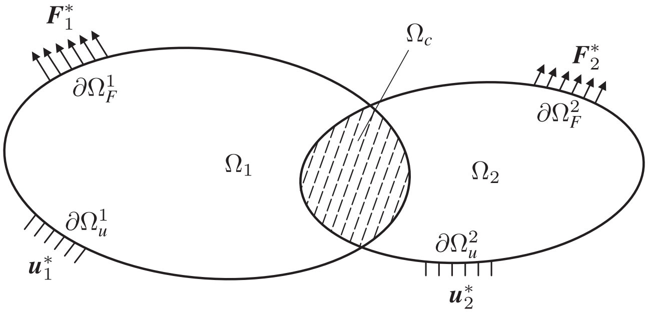

FIGURE 1 | Subdomains Ω_1 and Ω_2 and the coupling zone Ω_c.

The Arlequin method ensures the coupling of the two subdomains by using Lagrange multipliers. Constraints are imposed to enforce the continuity of displacements and force equilibrium in the overlap region. In this context, the total energy is composed of energy contributions from the coarse-scale model, assumed in region Ω_1, and the fine-scale model, assumed in region Ω_2, and the overlapping region Ω_c where both models interact. In the following, the method is illustrated for an elastic problem under small perturbations. The total energy functional of the coupling subdomains is given by [91, 107]:

$$\mathcal{E}\left(\boldsymbol{u}_1, \boldsymbol{u}_2, \lambda_u\right) = \mathcal{E}_1(\boldsymbol{u}_1) + \mathcal{E}_2(\boldsymbol{u}_2) + \mathcal{C}_u(\lambda_u, \boldsymbol{u}_1 - \boldsymbol{u}_2) \tag{21}$$

where $\boldsymbol{u}_1$ and $\boldsymbol{u}_2$ are the displacement fields corresponding to the subdomains Ω_1 and Ω_2, respectively, such that:

$$\boldsymbol{u}_i \in \mathcal{U}_i = \left\{\boldsymbol{u}_i \in H^1(\Omega_i) \mid \boldsymbol{u}_i = \boldsymbol{u}_i^* \quad \text{on} \quad \partial\Omega_u^i\right\}, \quad i = 1, 2 \tag{22}$$

where $\mathcal{U}_1$ and $\mathcal{U}_2$ represent the spaces of the kinematically admissible displacements fields $\boldsymbol{u}_1$ and $\boldsymbol{u}_2$. $\mathcal{E}_1(\boldsymbol{u}_1)$ and $\mathcal{E}_2(\boldsymbol{u}_2)$ refer to the potential energies corresponding to the subdomains Ω_1 and Ω_2, respectively. $\mathcal{C}_u(\lambda_u, \boldsymbol{u}_1 - \boldsymbol{u}_2)$ is the linear coupling operator, in which λ_u is the Lagrange multiplier defined in the coupling zone Ω_c, expressed by [91, 107]:

$$\mathcal{C}_u(\lambda_u, \boldsymbol{u}_1 - \boldsymbol{u}_2) = \int_{\Omega_c} \lambda_u \cdot (\boldsymbol{u}_1 - \boldsymbol{u}_2) + \ell_u^2 \boldsymbol{\varepsilon}(\lambda_u) : \boldsymbol{\varepsilon}(\boldsymbol{u}_1 - \boldsymbol{u}_2) d\Omega \tag{23}$$

where ℓ_u is a scaling parameter with dimension of length and $\boldsymbol{\varepsilon}(\cdot) = \frac{1}{2}\left(\nabla(\cdot) + \nabla^T(\cdot)\right)$. The coupling term in Equation (23) is known as the H^1 coupling, which involves both displacement and strain fields. It defines a natural scalar product on the Sobolev space $H^1(\Omega_c)$ [108]. When setting $\ell_u = 0$, the coupling operator in Equation (23) becomes the L^2 coupling, which involves only the displacement field. It defines a scalar product on the Lebesgue space $L^2(\Omega_c)$. A detailed discussion of these coupling terms can be found in Reference [93].

To avoid counting twice the energy in the overlapping region Ω_c and to satisfy the conservation of energy principle, the Arlequin method, in a variational framework, involves using weight functions to distribute the energy between the two models. The potential energies $\mathcal{E}_1(\boldsymbol{u}_1)$ and $\mathcal{E}_2(\boldsymbol{u}_2)$ corresponding to the subdomains Ω_1 and Ω_2, respectively, are expressed as:

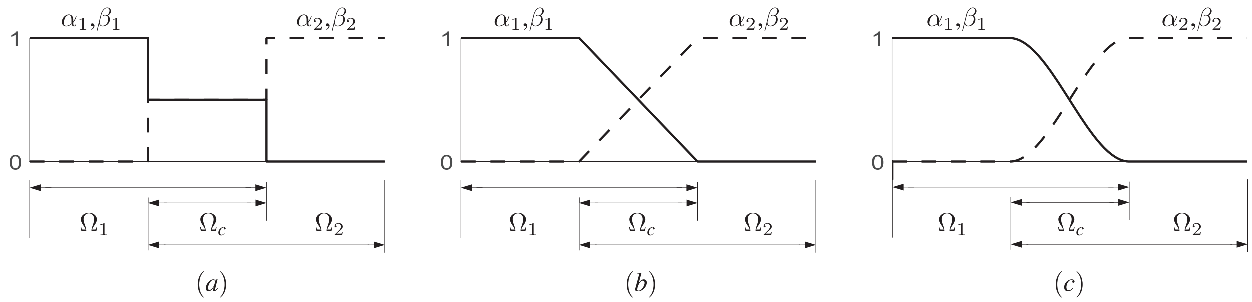

FIGURE 2 | Weight functions α_i and β_i: (*a*) constant, (*b*) linear, and (*c*) cubic.

$$
\begin{aligned}
\mathcal{E}_i(\boldsymbol{u}_i) = &\int_{\Omega_i} \alpha_i \boldsymbol{\sigma}(\boldsymbol{u}_i) : \boldsymbol{\varepsilon}(\boldsymbol{u}_i) d\Omega \\
&- \int_{\Omega_i} \beta_i \boldsymbol{f}^* \cdot \boldsymbol{u}_i d\Omega \\
&- \int_{\partial\Omega_F^i} \beta_i \boldsymbol{F}_i^* \cdot \boldsymbol{u}_i dS, \quad i = 1, 2
\end{aligned}
\tag{24}
$$

where $\boldsymbol{\sigma}$ and $\boldsymbol{\varepsilon}$ refer to the second-order Cauchy stress and strain tensors, respectively. $\boldsymbol{f}^*$ are the body forces, $\boldsymbol{F}_1^*$ and $\boldsymbol{F}_2^*$ are the prescribed forces on the boundaries $\partial\Omega_F^1$ and $\partial\Omega_F^2$, respectively, and α_i and β_i represent the weight functions for the elastic energy and the external forces work corresponding to the subdomains Ω_1 and Ω_2. These weight functions can be considered as a partition of unity satisfying the following relations:

$$
\alpha_1 = \beta_1 = 1 \quad \text{in} \quad \Omega_1 \setminus \Omega_c \tag{25}
$$

$$
\alpha_2 = \beta_2 = 1 \quad \text{in} \quad \Omega_2 \setminus \Omega_c \tag{26}
$$

$$
\alpha_1 + \alpha_2 = \beta_1 + \beta_2 = 1 \quad \text{in} \quad \Omega_c \tag{27}
$$

Several possible definitions of weight functions can be found in the literature (see, e.g., [109]). Figure 2 illustrates examples of weight functions. In this work, the same weight functions are used for the elastic energy and the work of external forces.

The minimization of the total energy functional in Equation (21) with respect to the fields $\boldsymbol{u}_1$, $\boldsymbol{u}_2$ and λ_u is expressed as: Find $(\boldsymbol{u}_1, \boldsymbol{u}_2, \lambda_u) \in \mathcal{U}_1 \times \mathcal{U}_2 \times \mathcal{U}_\lambda$ such that $\forall(\delta\boldsymbol{u}_1, \delta\boldsymbol{u}_2, \delta\lambda_u) \in \mathcal{U}_1^0 \times \mathcal{U}_2^0 \times \mathcal{U}_\lambda^0$,

$$
\begin{aligned}
&\int_{\Omega_1} \alpha_1 \boldsymbol{\sigma}(\boldsymbol{u}_1) : \boldsymbol{\varepsilon}(\delta\boldsymbol{u}_1) d\Omega + C_u(\lambda_u, \delta\boldsymbol{u}_1) \\
&\quad = \int_{\Omega_1} \alpha_1 \boldsymbol{f}^* \cdot \delta\boldsymbol{u}_1 d\Omega + \int_{\partial\Omega_F^1} \alpha_1 \boldsymbol{F}_1^* \cdot \delta\boldsymbol{u}_1 dS \\
&\int_{\Omega_2} \alpha_2 \boldsymbol{\sigma}(\boldsymbol{u}_2) : \boldsymbol{\varepsilon}(\delta\boldsymbol{u}_2) d\Omega - C_u(\lambda_u, \delta\boldsymbol{u}_2) \\
&\quad = \int_{\Omega_2} \alpha_2 \boldsymbol{f}^* \cdot \delta\boldsymbol{u}_2 d\Omega + \int_{\partial\Omega_F^2} \alpha_2 \boldsymbol{F}_2^* \cdot \delta\boldsymbol{u}_2 dS \\
&\int_{\Omega_c} \delta\lambda_u \cdot \boldsymbol{u}_1 + \ell_u^2 \boldsymbol{\varepsilon}(\delta\lambda_u) : \boldsymbol{\varepsilon}(\boldsymbol{u}_1) d\Omega \\
&\quad - \int_{\Omega_c} \delta\lambda_u \cdot \boldsymbol{u}_2 + \ell_u^2 \boldsymbol{\varepsilon}(\delta\lambda_u) : \boldsymbol{\varepsilon}(\boldsymbol{u}_2) d\Omega = 0
\end{aligned}
\tag{28}
$$

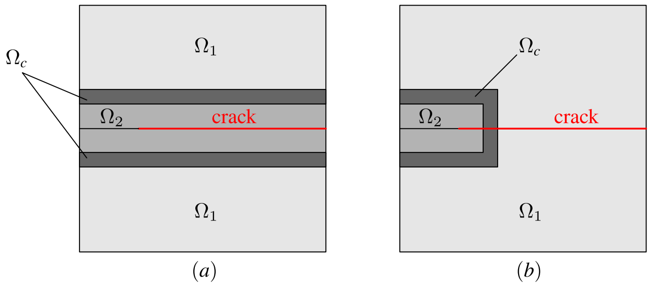

FIGURE 3 | (*a*) Crack initiation and propagation in the fine mesh region Ω_2, (*b*) Crack initiation in fine mesh region Ω_2 with propagation into coarse mesh region Ω_1 through the coupling zone Ω_c.

in which $\mathcal{U}_1^0$ and $\mathcal{U}_2^0$ refer to the spaces of the displacement fields $\delta\boldsymbol{u}_1$ and $\delta\boldsymbol{u}_2$ variations, respectively, expressed as:

$$
\mathcal{U}_i^0 = \left\{ \delta\boldsymbol{u}_i \in H^1(\Omega_i) \mid \delta\boldsymbol{u}_i = 0 \quad \text{on} \quad \partial\Omega_u^i \right\}, \quad i = 1, 2 \tag{29}
$$

$\mathcal{U}_\lambda$ and $\mathcal{U}_\lambda^0$ denote the spaces of Lagrange multiplier fields and their variations, respectively. The selection of the Lagrange multiplier spaces and the finite-element discretization is a crucial aspect of the Arlequin framework. A natural choice is to use the same spaces as well as the same continuous shape functions as those used for the displacement fields [91, 107]. Here, two possible approaches for model coupling can be used. The first one involves using the fine-mesh for the Lagrange multiplier fields discretization. This approach can lead to the locking phenomenon, where the fine-mesh solution is constrained or "locked" to the coarse-mesh (see [93] for more details). The second approach allows for avoiding this issue by using coarse Lagrange multiplier fields, in which the coarse-mesh is employed for the finite-element discretization of the Lagrange multipliers [91, 93, 107]. In this work, the second approach is adopted.

4 | Application of the Arlequin Method to Material Fracture Using the Phase Field Approach

The main idea of the proposed approach is to consider overlapped subdomains discretized with different mesh sizes. Fine meshes are employed in the regions of interest to model localized damage and capture accurately cracks initiation, and a coarse mesh is used elsewhere to optimize the computational costs. Initially, the method is developed for the case where cracks initiate and propagate in the fine regions only (see Figure 3a). This case is presented as an initial validation of the proposed method and is limited to the crack nucleation study. If the analysis includes both crack nucleation and propagation leading to material failure, a larger fine mesh region is required. However, this approach results in a significant increase in computational costs, as a finer mesh is used to model the crack evolution in the material. For a more general case, the method is extended to simulate crack nucleation in the fine mesh regions, allowing for their propagation into the coarse mesh region as well through the coupling zone, which is the significant contribution of this work (see Figure 3b).

4.1 | Case 1: Crack Initiation and Propagation in the Fine Mesh Region

In this section, the first case is considered, where a crack initiates and propagates in the fine mesh region only (see Figure 3a). The coupled displacement problem is solved taking into account the interaction between the subdomains. However, the damage problem is solved only in the fine regions, assuming that the coarse mesh subdomain remains undamaged. Considering the configuration in Figure 1, the total energy functional for this case is introduced as:

$$\mathcal{E}\left(\boldsymbol{u}_1, \boldsymbol{u}_2, d, \lambda_u\right) = \mathcal{E}_1(\boldsymbol{u}_1) + \mathcal{E}_2(\boldsymbol{u}_2, d) + C_u(\lambda_u, \boldsymbol{u}_1 - \boldsymbol{u}_2) \tag{30}$$

where $\boldsymbol{u}_1$ is the displacements field corresponding to the undamaged subdomain Ω_1, $\boldsymbol{u}_2$ and d refer to the displacements field and the phase field variable corresponding to the damaged subdomain Ω_2. λ_u and $C_u(\lambda_u, \boldsymbol{u}_1 - \boldsymbol{u}_2)$ are the Lagrange multipliers and the coupling operator for the mechanical problem coupling. $\mathcal{E}_1(\boldsymbol{u}_1)$ and $\mathcal{E}_2(\boldsymbol{u}_2, d)$ are the potential energies of the undamaged subdomain Ω_1 and the damaged subdomain Ω_2, respectively, expressed as:

$$\begin{aligned}\mathcal{E}_1(\boldsymbol{u}_1) = &\int_{\Omega_1} \alpha_1 \boldsymbol{\varepsilon}(\boldsymbol{u}_1) : \mathbb{C}_0 : \boldsymbol{\varepsilon}(\boldsymbol{u}_1) d\Omega - \int_{\Omega_1} \alpha_1 \boldsymbol{f}^* \cdot \boldsymbol{u}_1 d\Omega \\ &+ \int_{\partial\Omega_F^1} \alpha_1 \boldsymbol{F}_1^* \cdot \boldsymbol{u}_1 dS\end{aligned} \tag{31}$$

$$\begin{aligned}\mathcal{E}_2(\boldsymbol{u}_2, d) = &\int_{\Omega_2} \alpha_2 \boldsymbol{\varepsilon}(\boldsymbol{u}_2) : \mathbb{C}(d) : \boldsymbol{\varepsilon}(\boldsymbol{u}_2) \\ &+ \alpha_2 \psi_c \left(d^2 + \ell_0^2 \nabla d \cdot \nabla d\right) d\Omega \\ &- \int_{\Omega_2} \alpha_2 \boldsymbol{f}^* \cdot \boldsymbol{u}_2 d\Omega + \int_{\partial\Omega_F^2} \alpha_2 \boldsymbol{F}_2^* \cdot \boldsymbol{u}_2 dS\end{aligned} \tag{32}$$

where $\mathbb{C}_0$ is the undamaged stiffness tensor corresponding to the subdomain Ω_1 and $\mathbb{C}(d)$ is the damaged stiffness tensors corresponding to the subdomains Ω_2.

4.1.1 | Damage Problem

Given the displacement field $\boldsymbol{u}_2$, the minimization of the total energy functional (30) with respect to the damage field is expressed as: Find $d \in \mathcal{D}$ such that $\forall \delta d \in \mathcal{D}^0$,

$$\int_{\Omega_2} \alpha_2 (\mathcal{H} + \psi_c) d \delta d d\Omega + \alpha_2 \psi_c \ell_0^2 \nabla d \nabla(\delta d) d\Omega = \int_{\Omega_2} \alpha_2 \mathcal{H} \delta d d\Omega \tag{33}$$

where $\mathcal{H}$ is the history of energy corresponding to the subdomain Ω_2 defined as:

$$\mathcal{H} = \max_{\tau \in [0,t]} \left[\langle \psi_e^{+2}(\varepsilon;\ \tau) - \psi_c \rangle_+ \right] \tag{34}$$

in which ψ_e^{+2} denotes the positive part of the elastic energy density, given in Equation (3), corresponding to the damaged subdomain Ω_2.

The damage field d, the damage gradient, and their variations are approximated in one element by:

$$d = \boldsymbol{N}_d^2 d_i \quad ; \quad \delta d = \boldsymbol{N}_d^2 \delta d_i \quad ; \quad \nabla d = \boldsymbol{B}_d^2 d_i \quad ; \quad \nabla(\delta d) = \boldsymbol{B}_d^2 \delta d_i \tag{35}$$

where d_i are the nodal values of the damage field d, $\boldsymbol{N}_d^2$ and $\boldsymbol{B}_d^2$ are matrices of shape functions and shape functions derivatives for scalar fields, respectively, corresponding to the fine-mesh associated to the subdomains Ω_2. Here, 4-node elements are used for damage discretization (see Appendix A.1 for definitions of matrices and elements).

The discretization of the damage problem (33) using Equations (35) leads to the following discrete system of equations:

$$\boldsymbol{K}_d d = \boldsymbol{F}_d \tag{36}$$

in which

$$\boldsymbol{K}_d = \int_{\Omega_2} \alpha_2 (\mathcal{H} + \psi_c) \boldsymbol{N}_d^{2\,T} \boldsymbol{N}_d^2 d\Omega + \alpha_2 \psi_c \ell_0^2 \boldsymbol{B}_d^{2\,T} \boldsymbol{B}_d^2 d\Omega \tag{37}$$

$$\boldsymbol{F}_d = \int_{\Omega_2} \alpha_2 \boldsymbol{N}_d^{2\,T} \mathcal{H} d\Omega \tag{38}$$

4.1.2 | Mechanical Problem

Given the damage fields d, The minimization of the total energy function (30) with respect to the fields $\boldsymbol{u}_1$, $\boldsymbol{u}_2$ and λ is expressed as: find $\left(\boldsymbol{u}_1, \boldsymbol{u}_2, \lambda\right) \in \mathcal{U}_1 \times \mathcal{U}_2 \times \mathcal{U}_{\lambda_u}$ such that $\forall \left(\delta \boldsymbol{u}_1, \delta \boldsymbol{u}_2, \delta \lambda_u\right) \in \mathcal{U}_1^0 \times \mathcal{U}_2^0 \times \mathcal{U}_\lambda^0$,

$$\begin{aligned}&\int_{\Omega_1} \alpha_1 \boldsymbol{\varepsilon}(\boldsymbol{u}_1) : \mathbb{C}_0 : \boldsymbol{\varepsilon}(\delta \boldsymbol{u}_1) d\Omega + C(\lambda_u, \delta \boldsymbol{u}_1) \\ &\quad = \int_{\Omega_1} \alpha_1 \boldsymbol{f}^* \cdot \delta \boldsymbol{u}_1 d\Omega + \int_{\partial\Omega_F^1} \alpha_1 \boldsymbol{F}_1^* \cdot \delta \boldsymbol{u}_1 dS \\ &\int_{\Omega_2} \alpha_2 \boldsymbol{\varepsilon}(\boldsymbol{u}_2) : \mathbb{C}(d) : \boldsymbol{\varepsilon}(\delta \boldsymbol{u}_2) d\Omega - C(\lambda_u, \delta \boldsymbol{u}_2) \\ &\quad = \int_{\Omega_2} \alpha_2 \boldsymbol{f}^* \cdot \delta \boldsymbol{u}_2 d\Omega + \int_{\partial\Omega_F^2} \alpha_2 \boldsymbol{F}_2^* \cdot \delta \boldsymbol{u}_2 dS \\ &\int_{\Omega_c} \delta \lambda_u \cdot \boldsymbol{u}_1 + \ell_u^2 \boldsymbol{\varepsilon}(\delta \lambda_u) : \boldsymbol{\varepsilon}(\boldsymbol{u}_1) d\Omega \\ &\quad - \int_{\Omega_c} \delta \lambda_u \cdot \boldsymbol{u}_2 + \ell_u^2 \boldsymbol{\varepsilon}(\delta \lambda_u) : \boldsymbol{\varepsilon}(\boldsymbol{u}_2) d\Omega = 0\end{aligned} \tag{39}$$

The displacement fields $\boldsymbol{u}_1$ and $\boldsymbol{u}_2$, the Lagrange multipliers λ_u, the strain tensor, and their variations can be approximated in one element by:

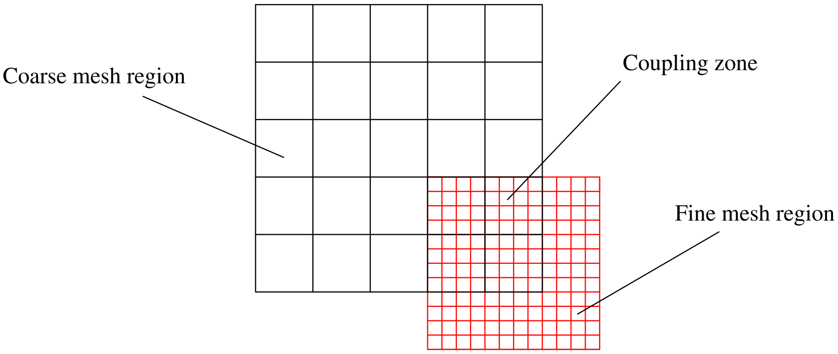

FIGURE 4 | Compatible mesh.

$$
\begin{aligned}
&\boldsymbol{u}_1 = \boldsymbol{N}_u^1 \boldsymbol{u}_1^i; \quad \delta \boldsymbol{u}_1 = \boldsymbol{N}_u^1 \delta \boldsymbol{u}_1^i; \quad \boldsymbol{\varepsilon}(\boldsymbol{u}_1) = \boldsymbol{B}_u^1 \boldsymbol{u}_1^i; \\
&\quad \boldsymbol{\varepsilon}(\delta \boldsymbol{u}_1) = \boldsymbol{B}_u^1 \delta \boldsymbol{u}_1^i \\
&\boldsymbol{u}_2 = \boldsymbol{N}_u^2 \boldsymbol{u}_2^i; \quad \delta \boldsymbol{u}_2 = \boldsymbol{N}_u^2 \delta \boldsymbol{u}_2^i; \quad \boldsymbol{\varepsilon}(\boldsymbol{u}_2) = \boldsymbol{B}_u^2 \boldsymbol{u}_2^i; \\
&\quad \boldsymbol{\varepsilon}(\delta \boldsymbol{u}_2) = \boldsymbol{B}_u^2 \delta \boldsymbol{u}_2^i \\
&\lambda_u = \boldsymbol{N}_u^1 \lambda_u^i; \quad \delta \lambda_u = \boldsymbol{N}_u^1 \delta \lambda_u^i; \quad \boldsymbol{\varepsilon}(\lambda_u) = \boldsymbol{B}_u^1 \lambda_u^i; \\
&\quad \boldsymbol{\varepsilon}(\delta \lambda_u) = \boldsymbol{B}_u^1 \delta \lambda_u^i
\end{aligned}
\tag{40}
$$

where $\boldsymbol{u}_1^i$, $\boldsymbol{u}_2^i$ and λ_u^i are the nodal values of the fields $\boldsymbol{u}_1$, $\boldsymbol{u}_2$ and λ_u. $\boldsymbol{N}_u^1$ and $\boldsymbol{B}_u^1$ are matrices of shape functions and shape functions derivatives for displacements and Lagrange multipliers fields $\boldsymbol{u}_1$ and λ_u corresponding to the coarse-mesh associated to the subdomain Ω_1. $\boldsymbol{N}_u^2$ and $\boldsymbol{B}_u^2$ are matrices of shape functions and shape functions derivatives for displacements field $\boldsymbol{u}_2$ corresponding to the fine-mesh associated to the subdomain Ω_2. Here, 4-node elements are used for discretizing the fields $\boldsymbol{u}_1$, $\boldsymbol{u}_2$ and λ_u.

The discretization of the mechanical problem (39) using Equations (40) leads to the following discrete system of equations:

$$
\begin{bmatrix} \mathbf{K}_u^1 & 0 & \mathbf{C}_u^{1^T} \\ 0 & \mathbf{K}_u^2 & -\mathbf{C}_u^{2^T} \\ \mathbf{C}_u^1 & -\mathbf{C}_u^2 & 0 \end{bmatrix}
\begin{bmatrix} \boldsymbol{U}_1 \\ \boldsymbol{U}_2 \\ \boldsymbol{\Lambda}_u \end{bmatrix}
=
\begin{bmatrix} \mathbf{F}_u^1 \\ \mathbf{F}_u^2 \\ 0 \end{bmatrix}
\tag{41}
$$

in which

$$
\boldsymbol{K}_u^1 = \int_{\Omega_1} \alpha_1 \boldsymbol{B}_u^{1^T} \boldsymbol{C}_0 \boldsymbol{B}_u^1 d\Omega \tag{42}
$$

$$
\boldsymbol{K}_u^2 = \int_{\Omega_2} \alpha_2 \boldsymbol{B}_u^{2^T} \boldsymbol{C}(d) \boldsymbol{B}_u^2 d\Omega \tag{43}
$$

$$
\boldsymbol{F}_u^1 = \int_{\Omega_1} \alpha_1 \boldsymbol{N}_u^{1^T} \boldsymbol{f}^* d\Omega + \int_{\partial \Omega_F^1} \alpha_1 \boldsymbol{N}_u^{1^T} \boldsymbol{F}_1^* dS \tag{44}
$$

$$
\boldsymbol{F}_u^2 = \int_{\Omega_2} \alpha_2 \boldsymbol{N}_u^{2^T} \boldsymbol{f}^* d\Omega + \int_{\partial \Omega_F^2} \alpha_2 \boldsymbol{N}_u^{2^T} \boldsymbol{F}_2^* dS \tag{45}
$$

$$
\boldsymbol{C}_u^1 = \int_{\Omega_c} \boldsymbol{N}_u^{1^T} \boldsymbol{N}_u^1 + \ell_u^2 \boldsymbol{B}_u^{1^T} \boldsymbol{B}_u^1 d\Omega \tag{46}
$$

$$
\boldsymbol{C}_u^2 = \int_{\Omega_c} \boldsymbol{N}_u^{1^T} \boldsymbol{N}_u^2 + \ell_u^2 \boldsymbol{B}_u^{1^T} \boldsymbol{B}_u^2 d\Omega \tag{47}
$$

The major difficulty of the Arlequin method lies in calculating the coupling matrices, especially the matrix $\boldsymbol{C}_u^2$ in Equation (47), due to the non-superposition of Gauss points in the overlapping region. In this work, for the sake of simplicity, regular and compatible meshes with 4-node quadrilateral elements are used (see Figure 4). The computation of the coupling matrices, in this case, is described in Appendix A.1.

4.1.3 | Algorithm 1

The first case algorithm is summarized in Algorithm 1.

4.2 | Case 2: Crack Initiation in Fine Mesh Regions With Propagation Into Coarse Mesh Region

The method is enhanced in this section to model the damage occurring in both fine and coarse mesh regions. Cracks initiate in the fine mesh regions and propagate through the coupling zone into the coarse mesh region (see Figure 3b). Both displacement and damage problems are solved considering the interaction between the subdomains. Considering the configuration in Figure 1, the total energy functional for this case is introduced as:

$$
\begin{aligned}
\mathcal{E}\left(\boldsymbol{u}_1, \boldsymbol{u}_2, d_1, d_2, \lambda_u, \lambda_d\right) = {} & \mathcal{E}_1(\boldsymbol{u}_1, d_1) + \mathcal{E}_2(\boldsymbol{u}_2, d_2) \\
& + C_u(\lambda_u, \boldsymbol{u}_1 - \boldsymbol{u}_2) \\
& + C_d(\lambda_d, d_1 - d_2)
\end{aligned}
\tag{48}
$$

where $\boldsymbol{u}_1$, d_1, $\boldsymbol{u}_2$ and d_2 are displacement and damage fields corresponding to the damaged subdomains Ω_1 and Ω_2, respectively. $\mathcal{E}_1(\boldsymbol{u}_1, d_1)$ and $\mathcal{E}_2(\boldsymbol{u}_2, d_2)$ are the potential energies of the damaged subdomains Ω_1 and Ω_2, respectively, expressed as:

$$
\begin{aligned}
\mathcal{E}_i(\boldsymbol{u}_i, d_i) = {} & \int_{\Omega_i} \alpha_i \boldsymbol{\varepsilon}(\boldsymbol{u}_i) : \mathbb{C}(d_i) : \boldsymbol{\varepsilon}(\boldsymbol{u}_i) \\
& + \alpha_i \psi_c \left(d_i^2 + \ell_0^2 \nabla d_i \cdot \nabla d_i\right) d\Omega \\
& - \int_{\Omega_i} \alpha_i \boldsymbol{f}^* \cdot \boldsymbol{u}_i d\Omega + \int_{\partial \Omega_F^i} \alpha_i \boldsymbol{F}_i^* \cdot \boldsymbol{u}_i dS, \quad i = 1, 2
\end{aligned}
\tag{49}
$$

λ_u and $C_u(\lambda_u, \boldsymbol{u}_1 - \boldsymbol{u}_2)$ are the Lagrange multipliers and the coupling operator, given in Equation (23), for the mechanical problem coupling. λ_d and $C_d(\lambda_u, d_1 - d_2)$ are the Lagrange

ALGORITHM 1 |

```
Define the geometry of the structure $\Omega$
Define the subdomains $\Omega_1$ and $\Omega_2$ and their mesh
Compute the coupling matrices $\boldsymbol{C}_u^1$ and $\boldsymbol{C}_u^2$ by (46), (47)
Initialize of the strain field $\boldsymbol{\varepsilon}(\boldsymbol{u}_2)$, the phase field $d$ and the energy history $\mathcal{H}$ corresponding to the subdomain $\Omega_2$
for $t_{n+1} \leq T$ do
    Given $\boldsymbol{\varepsilon}^n(\boldsymbol{u}_2)$, $d^n$ and $\mathcal{H}^n$ at load increment $t_n$
    Compute damage in the subdomain $\Omega_2$:
        Compute $\mathcal{H}^{n+1}(\varepsilon^n(\boldsymbol{u}_2), \mathcal{H}^n)$ by (11)
        Compute and assemble $K_d$ and $F_d$ by (37), (38)
        Compute damage $d^{n+1}$ by solving (36)
    Compute displacement :
        Compute $\boldsymbol{C}(d^{n+1})$ by (18)
        Compute and assemble $\boldsymbol{K}_u^1$, $\boldsymbol{K}_u^2$, $\boldsymbol{F}_u^1$ and $\boldsymbol{F}_u^2$ by (42)-(45)
        Compute displacement fields $\boldsymbol{u}_1^{n+1}$ and $\boldsymbol{u}_2^{n+1}$ by solving (41)
        Compute strain $\varepsilon^{n+1}(\boldsymbol{u}_2)$
end for
```

multipliers and the coupling operator for the damage problem coupling introduced here originally as:

$$C_d(\lambda_d, d_1 - d_2) = \int_{\Omega_c} \lambda_d \cdot (d_1 - d_2) + \ell_d^2 \nabla\lambda_d \cdot \nabla(d_1 - d_2) d\Omega \tag{50}$$

where ℓ_d is a scaling parameter with a dimension of length.

4.2.1 | Damage Problem

Given the displacement fields $\boldsymbol{u}_1$ and $\boldsymbol{u}_2$, The minimization of the total energy function (48) with respect to the fields d_1, d_2 and λ_d is expressed as: Find $(d_1, d_2, \lambda_d) \in \mathcal{D}_1 \times \mathcal{D}_2 \times \mathcal{D}_\lambda$ such that $\forall(\delta d_1, \delta d_2, \delta\lambda_d) \in \mathcal{D}_1^0 \times \mathcal{D}_2^0 \times \mathcal{D}_\lambda^0$,

$$\begin{aligned}
&\int_{\Omega_1} \alpha_1(\mathcal{H}_1 + \psi_c) d_1 \delta d_1 + \alpha_1 \psi_c \ell_0^2 \nabla d_1 \nabla(\delta d_1) d\Omega \\
&\quad + C_d(\lambda_d, \delta d_1) = \int_{\Omega_1} \alpha_1 \mathcal{H}_1 \delta d_1 d\Omega \\
&\int_{\Omega_2} \alpha_2(\mathcal{H}_2 + \psi_c) d_2 \delta d_2 + \alpha_2 \psi_c \ell_0^2 \nabla d_2 \nabla(\delta d_2) d\Omega \\
&\quad - C_d(\lambda_d, \delta d_2) = \int_{\Omega_2} \alpha_2 \mathcal{H}_2 \delta d_2 d\Omega \\
&\int_{\Omega_c} \delta\lambda_d \cdot d_1 + \nabla(\delta\lambda_d) \cdot \nabla d_1 d\Omega \\
&\quad - \int_{\Omega_c} \delta\lambda_d \cdot d_2 + \nabla(\delta\lambda_d) \cdot \nabla d_2 d\Omega = 0
\end{aligned} \tag{51}$$

where $\mathcal{H}_1$ and $\mathcal{H}_2$ are the history of energies corresponding to the subdomains Ω_1 and Ω_2, respectively, defined as:

$$\mathcal{H}_1 = \max_{\tau\in[0,t]} \left[\langle \psi_e^{+1}(\varepsilon;\ \tau) - \psi_c \rangle_+ \right] \tag{52}$$

$$\mathcal{H}_2 = \max_{\tau\in[0,t]} \left[\langle \psi_e^{+2}(\varepsilon;\ \tau) - \psi_c \rangle_+ \right] \tag{53}$$

in which ψ_e^{+1} and ψ_e^{+2} represent the positive part of the elastic energy densities, given in Equation (3), corresponding to the damaged subdomains Ω_1 and Ω_2, respectively. The selection of the spaces $\mathcal{D}_\lambda$ and $\mathcal{D}_\lambda^0$ follows the same strategy as that applied in the displacement problem. The coarse-mesh is considered for the discretization of the Lagrange multiplier field λ_d and its variation $\delta\lambda_d$.

The damage fields d_1 and d_2, the Lagrange multipliers λ_d, their gradients, and their variations are approximated in one element by:

$$\begin{aligned}
d_1 &= \boldsymbol{N}_d^1 d_1^i; \quad \delta d_1 = \boldsymbol{N}_d^1 \delta d_1^i; \quad \nabla d_1 = \boldsymbol{B}_d^1 d_1^i; \\
&\quad \nabla(\delta d_1) = \boldsymbol{B}_d^1 \delta d_1^i \\
d_2 &= \boldsymbol{N}_d^2 d_2^i; \quad \delta d_2 = \boldsymbol{N}_d^2 \delta d_2^i; \quad \nabla d_2 = \boldsymbol{B}_d^2 d_2^i; \\
&\quad \nabla(\delta d_2) = \boldsymbol{B}_d^2 \delta d_2^i \\
\lambda_d &= \boldsymbol{N}_d^1 \lambda_d^i; \quad \delta\lambda_d = \boldsymbol{N}_d^1 \delta\lambda_d^i; \quad \nabla\lambda_d = \boldsymbol{B}_d^1 \lambda_d^i; \\
&\quad \nabla(\delta\lambda_d) = \boldsymbol{B}_d^1 \delta\lambda_d^i
\end{aligned} \tag{54}$$

where d_1^i, d_2^i and λ_d^i are the nodal values of the fields d_1, d_2 and λ_d. $\boldsymbol{N}_d^1$ and $\boldsymbol{B}_d^1$ are matrices of shape functions and shape functions derivatives for scalar fields, respectively, corresponding to the coarse-mesh associated to the subdomains Ω_1. Here, 4-node elements are used to discretize the fields d_1, d_2 and λ_d.

The discretization of the damage problem (51) using Equations (54) leads to the following discrete system of equations:

$$\begin{bmatrix} \mathbf{K}_d^1 & 0 & \mathbf{C}_d^{1\,T} \\ 0 & \mathbf{K}_d^2 & -\mathbf{C}_d^{2\,T} \\ \mathbf{C}_d^1 & -\mathbf{C}_d^2 & 0 \end{bmatrix} \begin{bmatrix} D_1 \\ D_2 \\ \boldsymbol{\Lambda}_d \end{bmatrix} = \begin{bmatrix} \boldsymbol{F}_d^1 \\ \boldsymbol{F}_d^2 \\ 0 \end{bmatrix} \tag{55}$$

in which

$$\boldsymbol{K}_d^1 = \int_{\Omega_1} \alpha_1(\mathcal{H}_1 + \psi_c) \boldsymbol{N}_d^{1\,T} \boldsymbol{N}_d^1 + \alpha_1 \psi_c \ell_0^2 \boldsymbol{B}_d^{1\,T} \boldsymbol{B}_d^1 d\Omega \tag{56}$$

$$\boldsymbol{K}_d^2 = \int_{\Omega_2} \alpha_2(\mathcal{H}_2 + \psi_c) \boldsymbol{N}_d^{2\,T} \boldsymbol{N}_d^2 + \alpha_2 \psi_c \ell_0^2 \boldsymbol{B}_d^{2\,T} \boldsymbol{B}_d^2 d\Omega \tag{57}$$

$$\boldsymbol{F}_d^1 = \int_{\Omega_1} \alpha_1 \boldsymbol{N}_d^{1\,T} \mathcal{H}_1 d\Omega \tag{58}$$

ALGORITHM 2 |

```
Define the geometry of the structure $\Omega$.
Define the subdomains $\Omega_1$ and $\Omega_2$ and their mesh.
Compute the coupling matrices $\boldsymbol{C}_d^1$, $\boldsymbol{C}_d^2$, $\boldsymbol{C}_u^1$ and $\boldsymbol{C}_u^2$ by (60), (61), (46), and (47).
Initialize of the strain fields $\boldsymbol{\varepsilon}(\boldsymbol{u}_1)$ and $\boldsymbol{\varepsilon}(\boldsymbol{u}_2)$, the phase field variables $d_1$ and $d_2$ and the
    energy histories $\mathcal{H}_1$ and $\mathcal{H}_2$.
for $t_{n+1} \leq T$ do
    Given $\boldsymbol{\varepsilon}^n(\boldsymbol{u}_1)$, $\boldsymbol{\varepsilon}^n(\boldsymbol{u}_2)$, $d_1^n$, $d_2^n$, $\mathcal{H}_1^n$ and $\mathcal{H}_2^n$ at load increment $t_n$.
    Compute damage in the subdomain $\Omega_2$:
        Compute $\mathcal{H}_1^{n+1}(\varepsilon^n(\boldsymbol{u}_1), \mathcal{H}_1^n)$ and $\mathcal{H}_2^{n+1}(\varepsilon^n(\boldsymbol{u}_2), \mathcal{H}_2^n)$ by (11)
        Compute and assemble $\boldsymbol{K}_d^1$, $\boldsymbol{K}_d^2$, $\boldsymbol{F}_d^1$ and $\boldsymbol{F}_d^2$ by (56)-(59).
        Compute damage fields $d_1^{n+1}$ and $d_2^{n+1}$ by solving (55).
    Compute displacement :
        Compute $\boldsymbol{C}(d_1^{n+1})$ and $\boldsymbol{C}(d_2^{n+1})$ by (18).
        Compute and assemble $\boldsymbol{K}_u^1$, $\boldsymbol{K}_u^2$, $\boldsymbol{F}_u^1$ and $\boldsymbol{F}_u^2$ by (63), (64), (44), and (45).
        Compute displacement fields $\boldsymbol{u}_1^{n+1}$ and $\boldsymbol{u}_2^{n+1}$ by solving (41).
        Compute strain fields $\varepsilon^{n+1}(\boldsymbol{u}_2)$ and $\varepsilon^{n+1}(\boldsymbol{u}_1)$.
end for
```

$$\boldsymbol{F}_d^2 = \int_{\Omega_2} \alpha_2 \boldsymbol{N}_d^{2^T} \mathcal{H}_2 d\Omega \tag{59}$$

$$\boldsymbol{C}_d^1 = \int_{\Omega_c} \boldsymbol{N}_d^{1^T} \boldsymbol{N}_d^1 + \ell_d^2 \boldsymbol{B}_d^{1^T} B_d^1 d\Omega \tag{60}$$

$$\boldsymbol{C}_d^2 = \int_{\Omega_c} \boldsymbol{N}_d^{1^T} \boldsymbol{N}_d^2 + \ell_d^2 \boldsymbol{B}_d^{1^T} \boldsymbol{B}_d^2 d\Omega \tag{61}$$

4.2.2 | Mechanical Problem

Given the damage fields d_1 and d_2, The minimization of the total energy function (48) with respect to the fields $\boldsymbol{u}_1$, $\boldsymbol{u}_2$ and λ_u is expressed as: Find $(\boldsymbol{u}_1, \boldsymbol{u}_2, \lambda_u) \in \mathcal{U}_1 \times \mathcal{U}_2 \times \mathcal{U}_\lambda$ such that $\forall (\delta\boldsymbol{u}_1, \delta\boldsymbol{u}_2, \delta\lambda_u) \in \mathcal{U}_1^0 \times \mathcal{U}_2^0 \times \mathcal{U}_\lambda^0$,

$$\begin{aligned}
&\int_{\Omega_1} \alpha_1 \boldsymbol{\varepsilon}(\boldsymbol{u}_1) : \mathbb{C}(d_1) : \boldsymbol{\varepsilon}(\delta\boldsymbol{u}_1) d\Omega + \mathcal{C}(\lambda_u, \delta\boldsymbol{u}_1) \\
&\quad = \int_{\Omega_1} \alpha_1 \boldsymbol{f}^* \cdot \delta\boldsymbol{u}_1 d\Omega + \int_{\partial\Omega_F^1} \alpha_1 \boldsymbol{F}_1^* \cdot \delta\boldsymbol{u}_1 dS \\
&\int_{\Omega_2} \alpha_2 \boldsymbol{\varepsilon}(\boldsymbol{u}_2) : \mathbb{C}(d_2) : \boldsymbol{\varepsilon}(\delta\boldsymbol{u}_2) d\Omega - \mathcal{C}(\lambda_u, \delta\boldsymbol{u}_2) \\
&\quad = \int_{\Omega_2} \alpha_2 \boldsymbol{f}^* \cdot \delta\boldsymbol{u}_2 d\Omega + \int_{\partial\Omega_F^2} \alpha_2 \boldsymbol{F}_2^* \cdot \delta\boldsymbol{u}_2 dS \\
&\int_{\Omega_c} \delta\lambda_u \cdot \boldsymbol{u}_1 + \ell_c^2 \boldsymbol{\varepsilon}(\delta\lambda_u) : \boldsymbol{\varepsilon}(\boldsymbol{u}_1) d\Omega \\
&\qquad - \int_{\Omega_c} \delta\lambda_u \cdot \boldsymbol{u}_2 + \ell_c^2 \boldsymbol{\varepsilon}(\delta\lambda_u) : \boldsymbol{\varepsilon}(\boldsymbol{u}_2) d\Omega = 0
\end{aligned} \tag{62}$$

The discretization of the mechanical problem (62) using Equations (40) leads to the discrete system of equations in Equation (41), in which $\boldsymbol{K}_u^1$ and $\boldsymbol{K}_u^2$ are adjusted to:

$$\boldsymbol{K}_u^1 = \int_{\Omega_1} \alpha_1 B_u^{1^T} \boldsymbol{C}(d_1) B_u^1 d\Omega \tag{63}$$

$$\boldsymbol{K}_u^2 = \int_{\Omega_2} \alpha_2 B_u^{2^T} \boldsymbol{C}(d_2) B_u^2 d\Omega \tag{64}$$

4.2.3 | Algorithm 2

The second case algorithm is summarized in Algorithm 2.

5 | Numerical Applications

In this section, numerical applications for evaluating the accuracy and efficiency of the proposed Arlequin Phase field approach (A-PF) are presented. The first two examples are conducted using Algorithm 1, considering crack nucleation and propagation in the fine mesh region, while the remaining applications are performed using Algorithm 2, taking into account crack initiation in the fine mesh region and their propagation into the coarse mesh region. The method validation is carried out using phase field fracture simulations on finely meshed domains, in which the mesh size corresponds to the fine-mesh of the A-PF method. A comparison of computational times between the proposed approach and the reference computations is conducted for the first and third examples. This comparison is carried out using sequential algorithms with an HP Elitebook 850 G8 11th gen computer equipped with an i7-1185G7 processor and 64 GB of RAM.

5.1 | Notched Homogenous Plate (1)

In this first test, crack propagation in a notched homogeneous plate submitted to tensile loading is considered. The plate dimensions are $L \times H = 3 \times 1$ mm^2. The geometry and the boundary conditions, for the displacement problem, are depicted in Figure 5. The left end is fixed in both directions, and a uniform displacement U is applied on the right end of the domain in the x-direction. The computation is carried out with constant displacement increments $\Delta u = 3.10^{-7}$ mm for the first 400 time steps and $\Delta u = 2.5.10^{-8}$ mm for the remaining time steps. In this work, the mechanical properties used for all applications are as follows: $E = 52$ GPa, $\nu = 0.3$, and $\sigma_c = 0.03$ GPa. In this work, for the Arlequin framework, two subdomains are considered for all applications. In this example, the coarse mesh subdomain Ω_1, which is associated with the undamaged zone, is characterized by a coarse-mesh element size $h_{max} = 0.04$ mm, with a length $b = 1.44$ mm on each side. The fine mesh subdomain Ω_2, related to the damaged zone, is characterized by a fine-mesh element size $h_{min} = 0.0019$ mm and a width $a = 0.2$ mm. The notch length is $c = 0.5$ mm, and its width corresponds to the fine-mesh size h_{min}. the width of the coupling zone Ω_c corresponds to coarse-mesh size h_{max} (see Figure 5). In this example, the geometry is chosen so as to ensure crack nucleation and propagation solely in the fine mesh zone, where algorithm 1 is applied. Figure 6 illustrates the real mesh used in this application, in which the zoomed portion clearly shows the compatible mesh, featuring 21×21 fine elements embedded within a single coarse element. The regularization length for the damage problem is $\ell_0 = 2h_{min}$. In this work, the scaling parameter ℓ_u in Equation (23) used for the displacement problem coupling is chosen to be equal to h_{min} as in Reference [110].

Figure 7 shows the final damage state of the notched homogeneous domain, in which the red box indicates the fine mesh region. A very fine crack can be observed, demonstrating the high resolution used in this example. Figure 8a–f provide zoomed views of the notched homogeneous domain illustrating the crack evolution at displacements $U = 1.29.10^{-4}$ mm, $U = 1.41.10^{-4}$ mm and $U = 1.6.10^{-4}$ mm using the A-PF method (case 1) and the reference computation, respectively. Figure 9, compares the force-displacement curves of the A-PF (case 1) simulation and of the reference computation. An excellent agreement between both solutions can be noticed, which demonstrates the high accuracy of the A-PF method (case 1) in predicting crack nucleation and propagation. Furthermore, the A-PF method shows a high efficiency in terms of computation time. The total number of elements used for the A-PF (case 1) simulation, considering both subdomains, is $N_e = 56662$, while the reference calculation employs $N_e^{ref} = 826612$. The computation times for the A-PF method (case 1) and the reference calculation are $t = 3\text{h}31$ min and $t_{ref} = 39\text{h}04$ min, respectively (see Figure 18a). These results demonstrate the computation time optimization achieved with the A-PF method, while ensuring high accuracy in predicting crack nucleation and propagation.

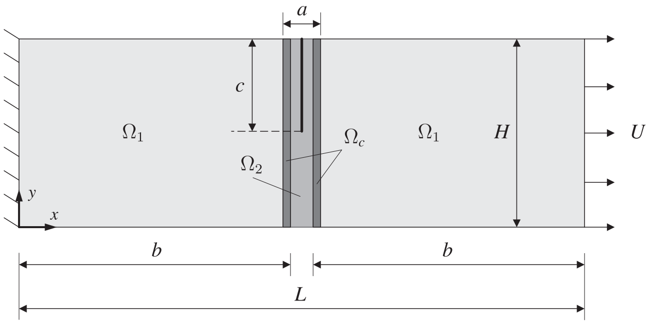

FIGURE 5 | Notched homogeneous plate in tension (1): Geometry and boundary conditions.

5.2 | Notched Porous Square Plate

In a second test, the effect of the crack nucleation on the overall damageable behavior of a notched porous square plate, submitted to tensile loading, is analyzed. Here, damage simulations are performed considering two configurations. In the first one, the crack tips are aligned with pores, from which cracks initiate (see Figure 10a). In the second situation, the pores are offset to force crack nucleation from the notch (see Figure 10b). The square plate dimensions are $L \times L = 1 \times 1$ mm^2, the pore radius is $r = 0.02$ mm, and the notch length is $c = 0.2$ mm. The geometry and the boundary conditions for both situations are depicted in Figure 10a,b. The bottom end is fixed in both directions, and a uniform displacement U is applied to the top end of the domain in the y-direction. The computation is carried out with constant displacement increments $\Delta u = 8.10^{-7}$ mm for the first 100 time steps and $\Delta u = 10^{-7}$ mm for the remaining time steps. The coarse-mesh associated with the undamaged subdomain Ω_1 is $h_{max} = 0.04$ mm. The length of both sides of the subdomain Ω_1

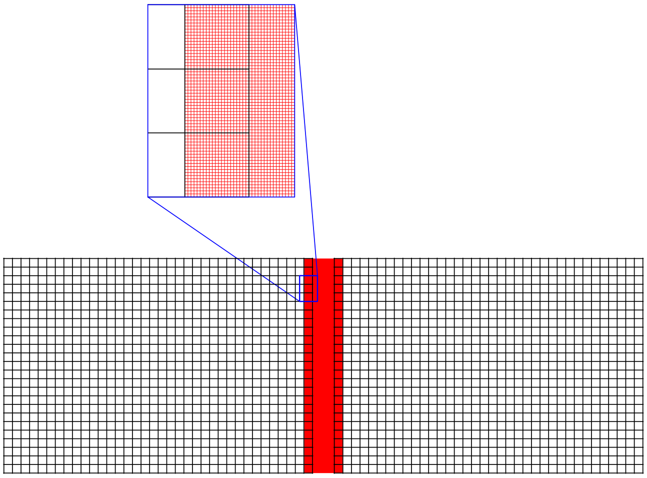

FIGURE 6 | Mesh used for the notched homogeneous plate (1) problem.

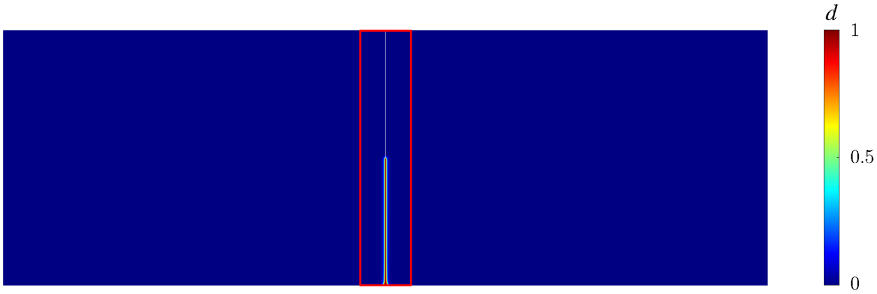

FIGURE 7 | Final damage state of the notched homogeneous plate (1) using the A-PF method (case 1). The red box indicates the fine mesh region.

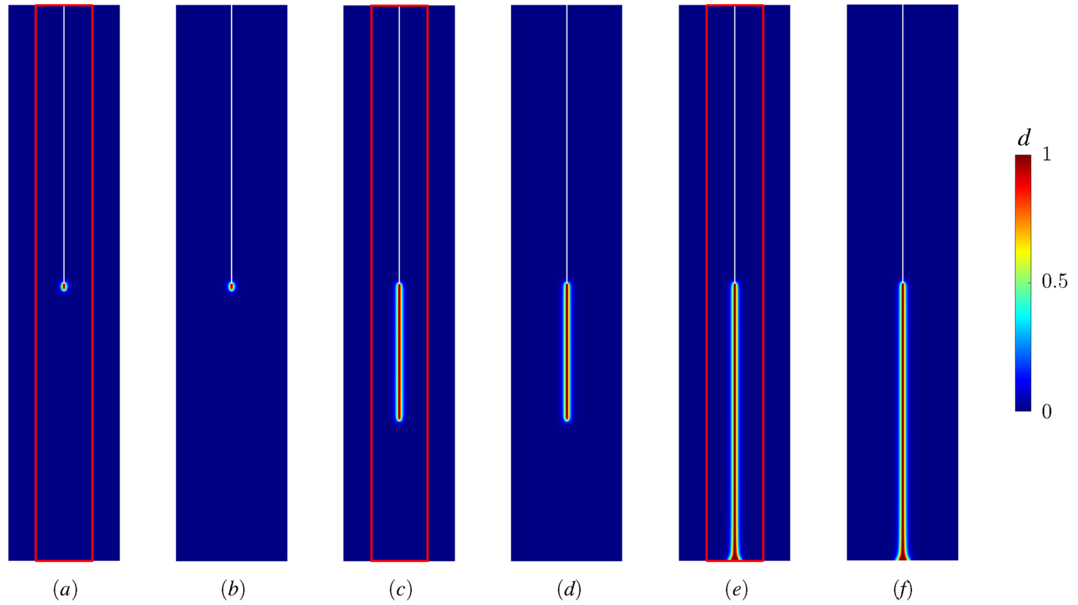

FIGURE 8 | Notched homogeneous plate (1): (a) and (b) A-PF (case 1) and reference solutions at displacement $U = 1.29.10^{-4}$ mm, respectively, (c) and (d) A-PF (case 1) and reference solutions at displacement $U = 1.41.10^{-4}$ mm, respectively, and (e) and (f) final damage states of the A-PF (case 1) simulation and the reference computation, respectively. The red box indicates the fine mesh region.

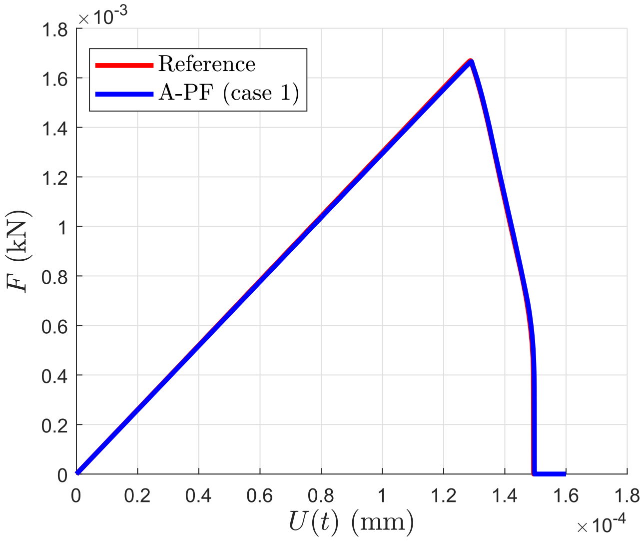

FIGURE 9 | Notched homogeneous plate (1): Force-displacement curves.

is $b = 0.44$ mm. The fine-mesh associated with the damaged subdomain Ω_2 is chosen as $h_{min} = 0.0027$ mm. The width of the subdomain Ω_2 is $a = 0.2$ mm, and the width of the coupling zone Ω_c corresponds to the size of the coarse-mesh h_{max}. Figure 11 illustrates the mesh used in this application for both configurations. The regularization length for the damage problem is $\ell_0 = 2h_{min}$.

Figure 12a,c illustrate crack nucleation in both situations: Initiation at pores and the notch, corresponding to displacements $U = 1.28.10^{-4}$ mm and $U = 1.06.10^{-4}$ mm, respectively. Figure 12b,d show crack evolution for both situations at the same displacement $U = 1.32.10^{-4}$ mm. A difference in crack nucleation time steps can be noted between the two situations. Cracks initiate earlier in the notch compared to pores. This observation is confirmed by force-displacement curves in Figure 13. Figure 13a shows the force evolution in the case of crack initiation at pores. Here, the force increases until reaching a peak, after which it starts decreasing. In contrast, Figure 13b illustrates the force evolution where cracks initiate at the notch. In this case, cracks initiate earlier than in the previous one, starting at the notch and propagating until reaching the first adjacent pore. The force decreases slightly before rising again to a new peak. Notably, the maximum force in the case of crack initiation at pores is greater than in the case where cracks initiate at the notch. This indicates that crack nucleation can significantly influence the overall damage behavior.

When comparing force-displacement curves of the A-PF method (case 1) and reference computations in Figure 13a,b, a significant agreement between solutions is remarkable, which demonstrates the high accuracy of the proposed method in predicting crack nucleation and tracking its propagation. The results of this example demonstrate the ability of the proposed method to accurately and efficiently predict crack nucleation and propagation, particularly in cases where the presence of fine details in the structure requires a refined mesh.

5.3 | Notched Homogeneous Plate (2)

In the third application, the key contribution of this work is illustrated: The modeling of crack nucleation in the fine mesh region, allowing its propagation into the coarse mesh region through the coupling zone, considering the Algorithm 2. Crack propagation in a notched homogeneous plate submitted to tensile loading is considered. The plate dimensions are $L \times H = 3 \times 1$ mm^2 and the notch length is $c = 0.25$ mm. Here, a patch of dimensions $a \times b = 0.2 \times 0.5$ mm^2 is considered, associated with the fine mesh region (see Figure 14). The coarse-mesh element size is

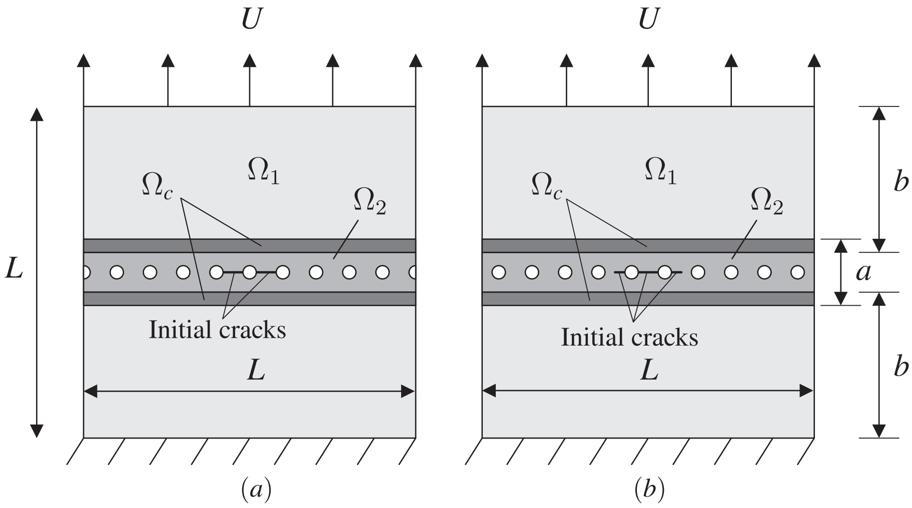

FIGURE 10 | Notched porous square plate (geometry and boundary conditions): (a) first configuration, (b) second configuration.

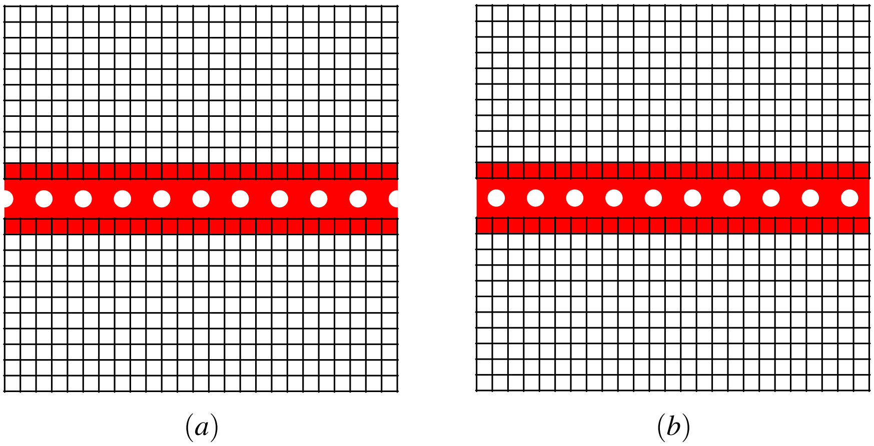

FIGURE 11 | Notched porous square plate mesh: (a) configuration 1, (b) configuration 2.

$h_{max} = 0.013$ mm and the fine-mesh element size is $h_{min} = 0.0027$ mm. The geometry and the boundary conditions, for the displacement problem, are depicted in Figure 14. The left end is fixed in both directions, and a uniform displacement U is applied to the right end of the domain in the x-direction. The computation is carried out with constant displacement increments $\Delta u = 1.5.10^{-6}$ mm for the first 200 time steps and $\Delta u = 2.5.10^{-7}$ mm for the remaining time steps. Figure 15 illustrates a zoom of the mesh used in this application, in which the compatible mesh can be observed with 5×5 fine elements embedded within one coarse element. In this work, the same regularization length is used for both coarse and fine regions, and it is chosen as $\ell_0 = 2h_{max}$. Using different regularization lengths in coarse and fine meshes is under investigation. Additionally, in this work, the scaling parameter ℓ_d for the damage problem coupling operator is chosen to correspond to the fine-mesh size as the displacement problem coupling operator. A study of the influence of key parameters within the proposed method, including the scaling parameter for the damage problem, is under investigation.

Figure 16a–f illustrate the crack evolution of the notched homogeneous domain at displacements $U = 4.19.10^{-4}$ mm, $U = 4.28.10^{-4}$ mm and $U = 5.10^{-4}$ mm using the A-PF method (case 1) and the reference computation, respectively. The damage solution shows a smooth transition from the fine mesh region to the coarse mesh region, thanks to the proposed damage problem coupling operator. This operator ensures the continuity of the damage fields across the coupling zone, preserving the consistency of the solution throughout the entire domain. Figure 17 compares force-displacement curves for the A-PF (case 2) simulation and the reference computation, indicating an excellent agreement between both solutions. Additionally, computation time is significantly reduced with the A-PF method (case 2). The total number of elements used for the A-PF (case 2) simulation, considering both subdomains, is $N_e = 30550$, while the number of elements used for the reference calculation is $N_e^{ref} = 421781$. The computation times for the A-PF method (case 2) and the reference calculation are $t = 1\text{h}02$ min and $t_{ref} = 9\text{h}11$ min, respectively (see Figure 18b). Computation time is significantly reduced with the A-PF method (case 2) compared with the finely meshed model. It demonstrates the high accuracy and efficiency of the proposed method in modeling crack nucleation and propagation for structural problems containing localized defects.

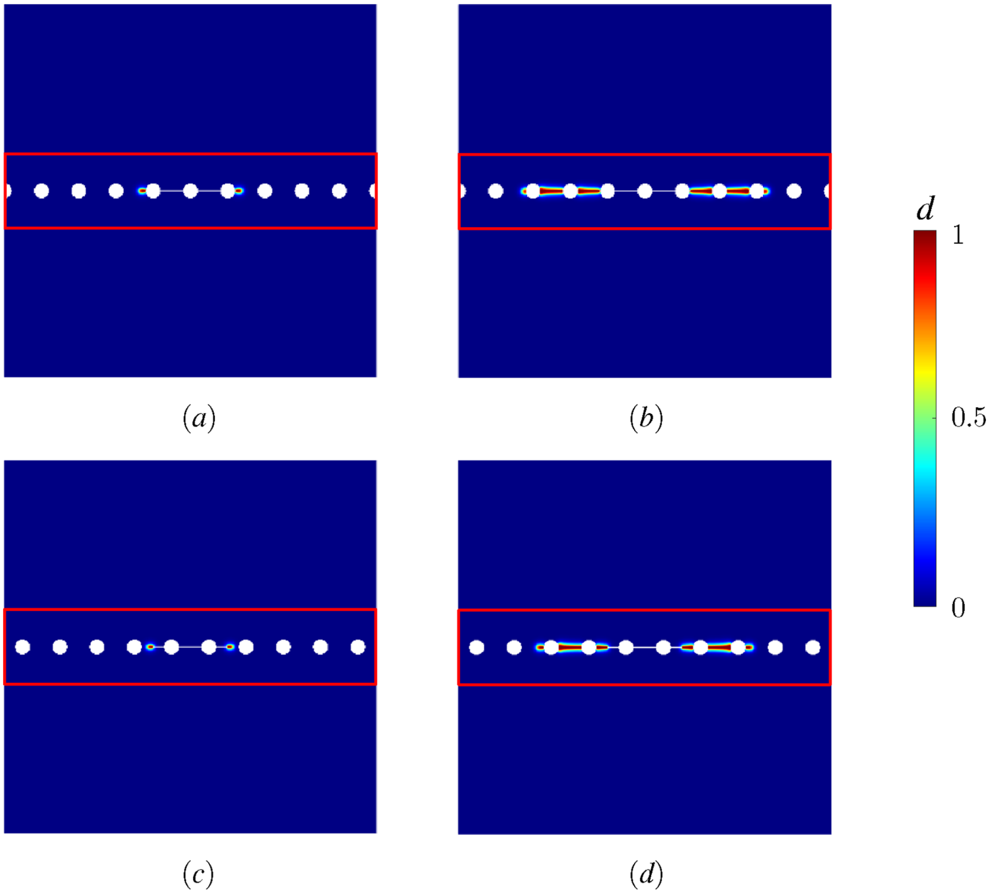

FIGURE 12 | Notched porous square plate: (a) and (b) A-PF (case 1) solutions at displacements $U = 1.28.10^{-4}$ mm and $U = 1.32.10^{-4}$ mm, respectively, in the case of cracks initiation at pores, (c) and (d) A-PF (case 1) solutions at displacements $U = 1.06.10^{-4}$ mm and $U = 1.32.10^{-4}$ mm, respectively, in the case of cracks initiation at the notch. The red box indicates the fine mesh region.

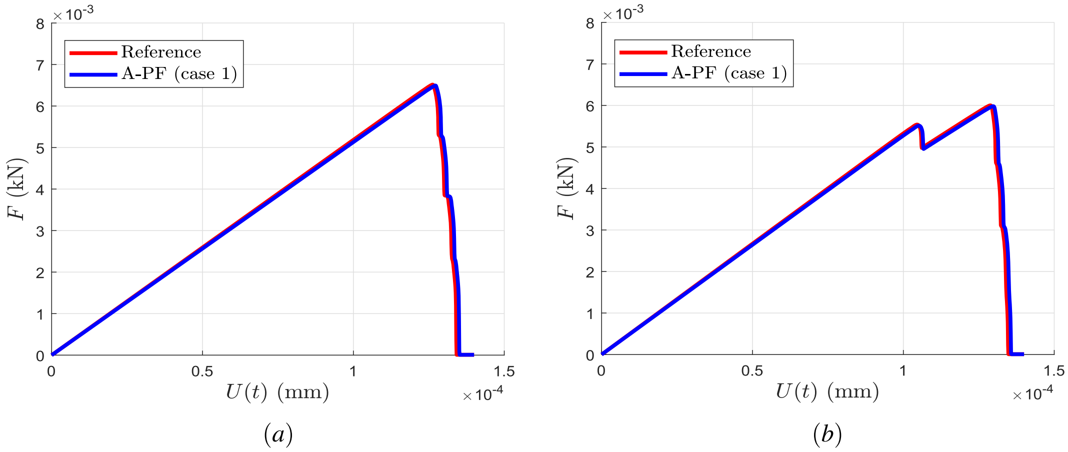

FIGURE 13 | Notched porous square plate: Force-displacement curves. (a) cracks initiate at pores, (b) cracks initiate at the notch.

5.4 | Perforated Square Plate

In this last example, crack nucleation and propagation in a perforated square plate, submitted to tensile and shear loading, are considered. The square plate dimensions are $L \times L = 1 \times 1$ mm^2 and the hole radius is $r = 0.07$ mm. The geometry and the boundary conditions, for the displacement problem, are depicted in Figure 19a,b. The bottom end is fixed in both directions, and a uniform displacement U is applied to the top end of the domain in the y-direction (tensile) or x-direction (shear). Left and right ends are blocked in the y-direction for the shear simulation. For the case of tensile loading, the computation is carried out with constant displacement increments $\Delta u = 2.2.10^{-6}$ mm for the first 100 time steps and $\Delta u = 2.10^{-7}$ mm for the remaining time steps.

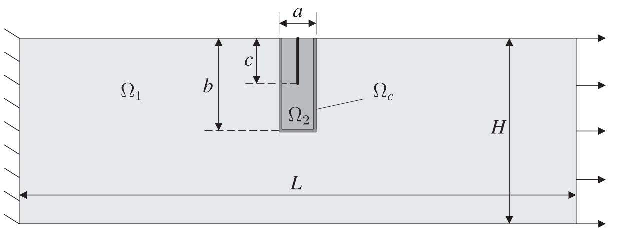

FIGURE 14 | Notched homogeneous plate (2): Geometry and boundary conditions.

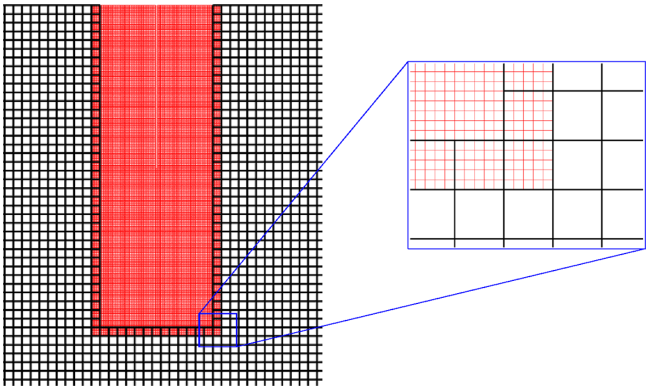

FIGURE 15 | Notched homogeneous plate (2) mesh.

For the shear simulation, the computation is carried out with constant displacement increments $\Delta u = 7.10^{-6}$ mm for the first 100 time steps and $\Delta u = 5.10^{-7}$ mm for the remaining time steps. The coarse-mesh and fine-mesh associated with the subdomains Ω_1 and Ω_2 are $h_{max} = 0.013$ mm and $h_{min} = 0.0027$, respectively. The width of the coupling zone Ω_c corresponds to one coarse element size h_{max}. Figure 20 depicts a zoom of the mesh used in this application for both loading cases. The regularization length for the damage problem is $\ell_0 = 2h_{max}$.

Figure 21a,b show crack evolution for the tensile loading case at displacements $U = 2.68.10^{-4}$ mm and $U = 2.71.10^{-4}$ mm, respectively. Figure 21c,d illustrate crack evolution for the shear loading case at displacements $U = 8.17.10^{-4}$ mm and $U = 8.39.10^{-4}$ mm, respectively. Figure 22a,b compare the force-displacement curves for tensile and shear simulation, respectively, corresponding to the A-PF method (case 2) and reference computations. An excellent agreement between solutions is again observed. Figure 23a,c show the final damage states obtained by the A-PF method (case 2), corresponding to tensile and shear simulations, respectively. Figure 23b,d show the final damage states obtained by reference computations, corresponding to tensile and shear simulations, respectively. This example demonstrates the high accuracy of the proposed approach in predicting crack nucleation and propagation in structures containing localized defects under varying loading conditions.

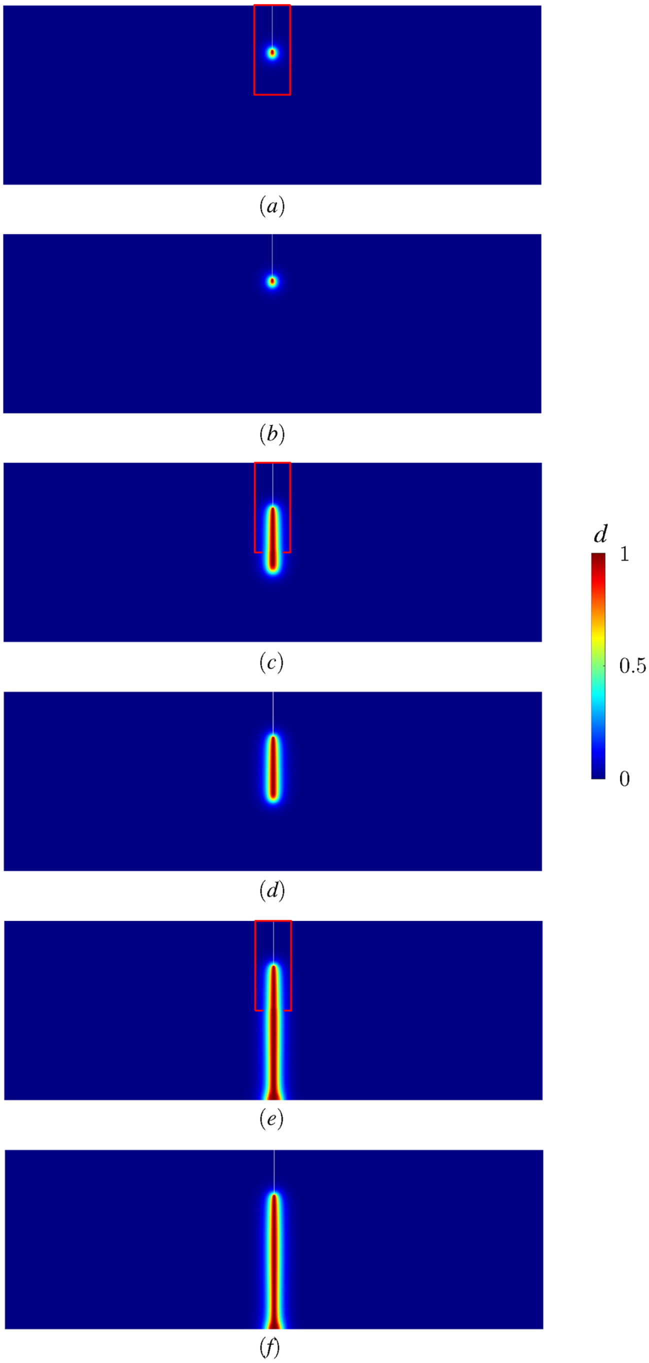

FIGURE 16 | Notched homogeneous plate (2): (a) and (b) A-PF (case 2) and reference solutions at displacement $U = 4.19.10^{-4}$ mm, respectively, (c) and (d) A-PF (case 2) and reference solutions at displacement $U = 4.28.10^{-4}$ mm, respectively, and (e) and (f) final damage states of the A-PF (case 2) simulation and the reference computation, respectively. The red box indicates the fine mesh region.

6 | Conclusion

In this work, a coarse mesh-fine mesh coupling framework with overlapping has been formulated for the phase field fracture problem. The method relies on the Arlequin method [91, 107], which is here extended and implemented within the phase field method to fracture, for cases where cracks can occur in both meshes, and propagate from the fine mesh to the coarse mesh. The novelties include the formulations developed for the phase field in this context and their implementation using finite elements.

A fine mesh is used in a region around a localized defect, where the initiation of cracks critically depends on an accurate description of the local defects (pores, initial cracks, etc.). A coarser mesh can be used to model the effects of boundary conditions if they are located far from defects, or to simulate the propagation of cracks once they have been initiated.

First, a simplified formulation has been proposed for cases where the cracks only initiate and propagate in the fine mesh. In this case, the formulation is based on a total energy whose part related to the coarse mesh remains elastic. A second formulation is developed, where the total energy includes the fracture energy of both fine and coarse meshes, allowing cracks to initiate in the fine mesh and then propagate in the coarse mesh. In both cases, the Arlequin framework is extended, in which variational coupling operators are developed to bridge the models in the overlapping regions between fine and coarse meshes. A staggered algorithmic solving procedure has been developed for both cases.

Results show an excellent agreement with reference solutions consisting of uniform fine meshes, while drastic computational gains can be achieved by using a coarse mesh far from the regions of defects. Perspectives of this work may include a more in-depth analysis of the effects of the different choices of the coupling operators.

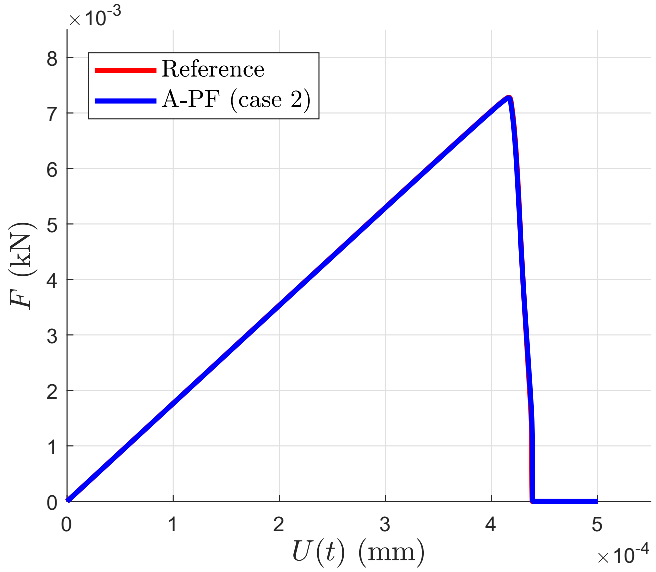

FIGURE 17 | Notched homogeneous plate (2): Force-displacement curves.

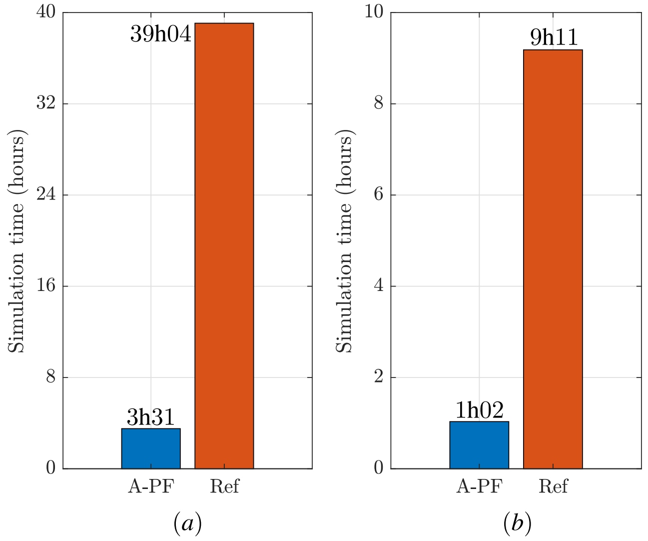

FIGURE 18 | Comparison of simulation times: (a) Notched homogeneous plate (1), (b) Notched homogeneous plate (2).

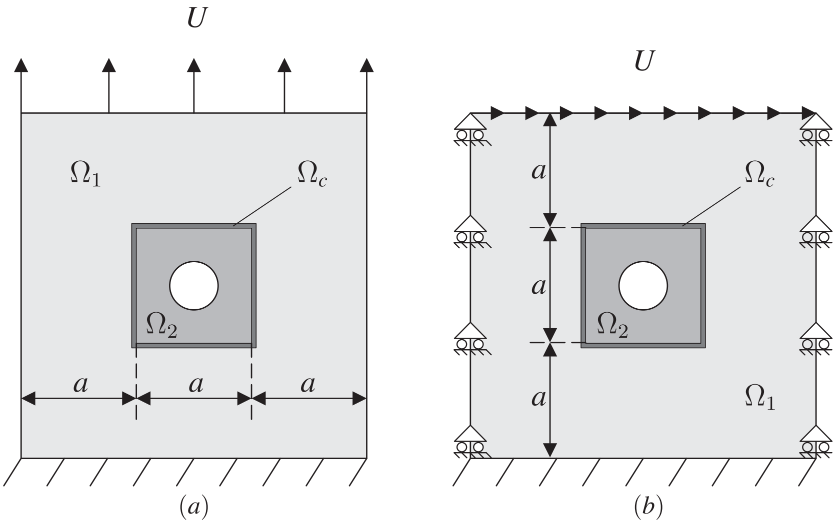

FIGURE 19 | Perforated square plate (geometry and boundary conditions): (a) Tensile loading, (b) Shear loading.

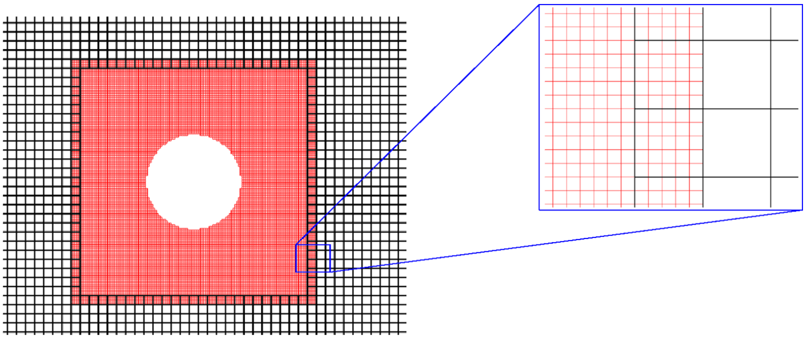

FIGURE 20 | Perforated square plate mesh.

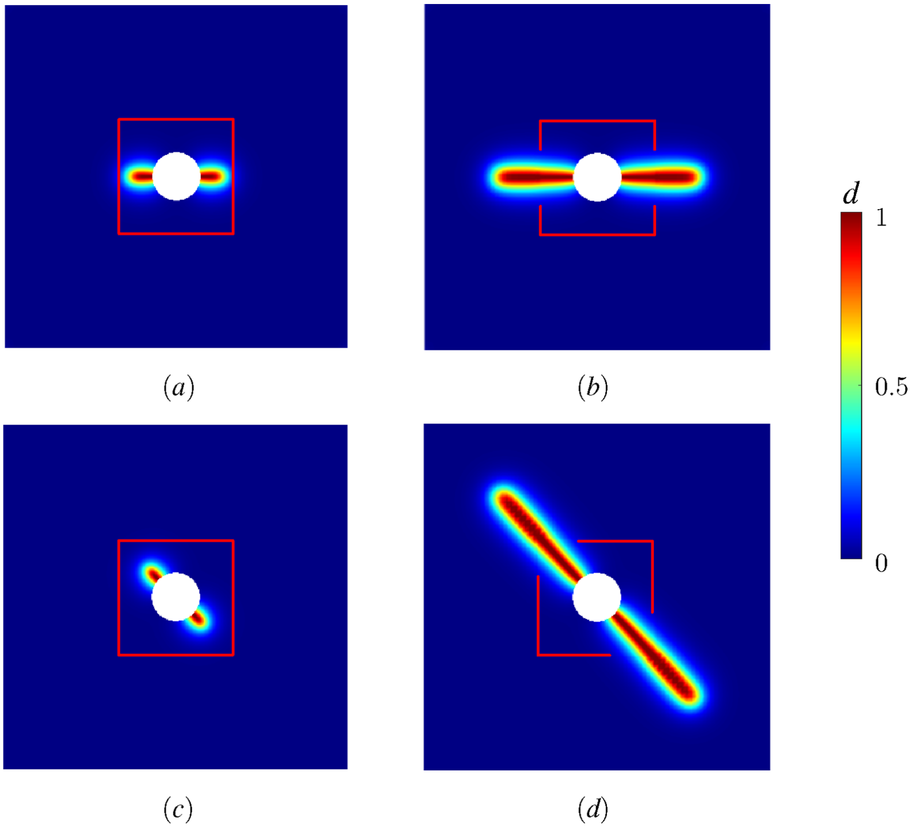

FIGURE 21 | Perforated square plate: (a) and (b) A-PF (case 2) solutions at displacements $U = 2.68.10^{-4}$ mm and $U = 2.71.10^{-4}$ mm, respectively, in the case of tensile loading, (c) and (d) A-PF (case 2) solutions at displacements $U = 8.17.10^{-4}$ mm and $U = 8.39.10^{-4}$ mm, respectively, in the case of shear loading. The red box indicates the fine mesh region.

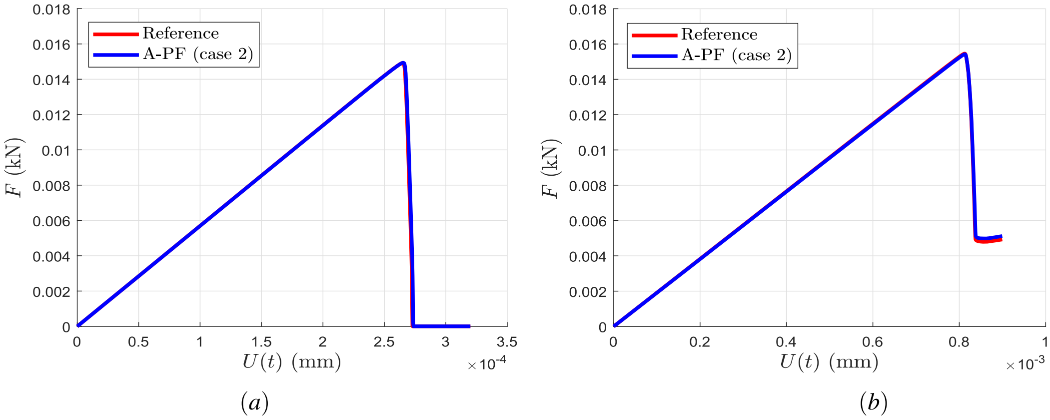

FIGURE 22 | Perforated square plate: Force-displacement curves (a) Tensile loading, (b) Shear loading.

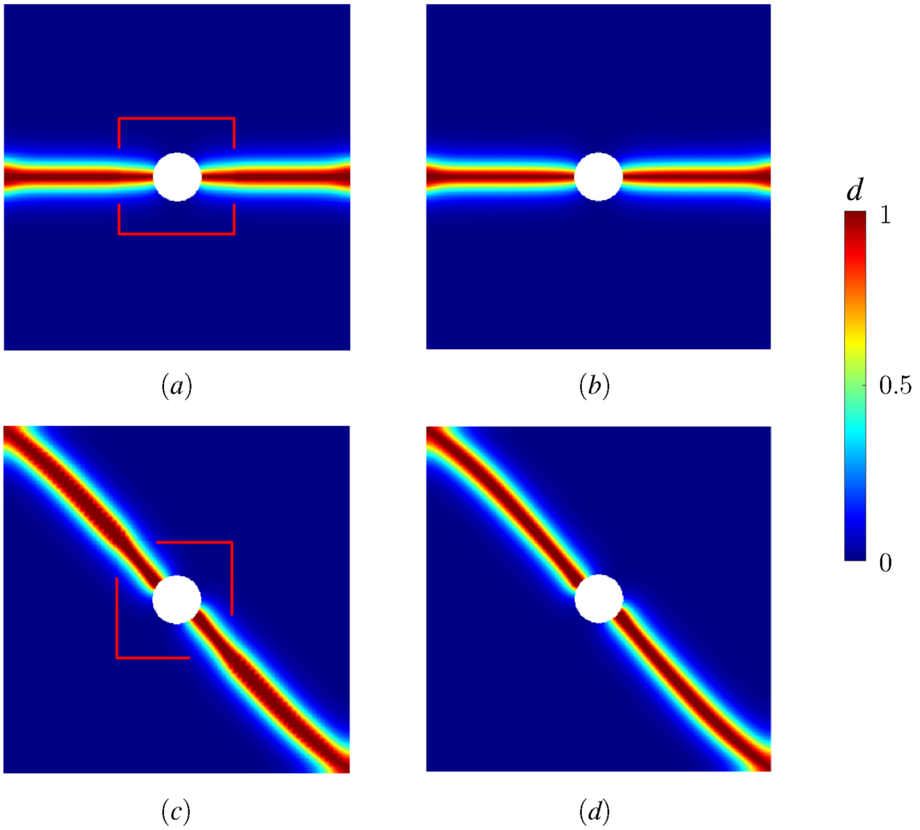

FIGURE 23 | Perforated square plate: (a) and (b) Final damage states of the A-PF (case 2) simulation and the reference computation, respectively, for the case of tensile loading, (c) and (d) Final damage states of the A-PF (case 2) simulation and the reference computation, respectively, for the case of shear loading. The red box indicates the fine mesh region.

Acknowledgments

The authors gratefully acknowledge the financial support from the LABEX Multi-Scale Modeling & Experimentation of Materials for Sustainable Construction (MMCD) through ANR Investments for the Future program ANR- 11-LABX-022-01.

Data Availability Statement

The data that support the findings of this study are available from the corresponding author upon reasonable request.

References

1. B. Bourdin, G. A. Francfort, and J.-J. Marigo, "Numerical Experiments in Revisited Brittle Fracture," *Journal of the Mechanics and Physics of Solids* 48, no. 4 (2000): 797–826.

2. G. A. Francfort and J.-J. Marigo, "Revisiting Brittle Fracture as an Energy Minimization Problem," *Journal of the Mechanics and Physics of Solids* 46, no. 8 (1998): 1319–1342.

3. G. Lancioni and G. Royer-Carfagni, "The Variational Approach to Fracture Mechanics. A Practical Application to the French Panthéon in Paris," *Journal of Elasticity* 95 (2009): 1–30.

4. H. Amor, J.-J. Marigo, and C. Maurini, "Regularized Formulation of the Variational Brittle Fracture With Unilateral Contact: Numerical Experiments," *Journal of the Mechanics and Physics of Solids* 57, no. 8 (2009): 1209–1229.

5. C. Miehe, M. Hofacker, L.-M. Schänzel, and F. Aldakheel, "Phase Field Modeling of Fracture in Multi-Physics Problems. Part II. Coupled Brittle-To-Ductile Failure Criteria and Crack Propagation in Thermo-Elastic–Plastic Solids," *Computer Methods in Applied Mechanics and Engineering* 294 (2015): 486–522.

6. C. Miehe, M. Hofacker, and F. Welschinger, "A Phase Field Model for Rate-Independent Crack Propagation: Robust Algorithmic Implementation Based on Operator Splits," *Computer Methods in Applied Mechanics and Engineering* 199 (2010): 2776–2778.

7. C. Miehe, L.-M. Schaenzel, and H. Ulmer, "Phase Field Modeling of Fracture in Multi-Physics Problems. Part I. Balance of Crack Surface and Failure Criteria for Brittle Crack Propagation in Thermo-Elastic Solids," *Computer Methods in Applied Mechanics and Engineering* 294 (2015): 449–485.

8. C. Miehe, F. Welschinger, and M. Hofacker, "Thermodynamically Consistent Phase-Field Models of Fracture: Variational Principles and Multi-Field FE Implementations," *International Journal for Numerical Methods in Engineering* 83, no. 10 (2010): 1273–1311.

9. K. Pham, H. Amor, J.-J. Marigo, and C. Maurini, "Gradient Damage Models and Their Use to Approximate Brittle Fracture," *International Journal of Damage Mechanics* 20, no. 4 (2011): 618–652.

10. M. Ambati, T. Gerasimov, and L. De Lorenzis, "A Review on Phase-Field Models of Brittle Fracture and a New Fast Hybrid Formulation," *Computational Mechanics* 55 (2015): 383–405.

11. M. J. Borden, T. J. Hughes, C. M. Landis, and C. V. Verhoosel, "A Higher-Order Phase-Field Model for Brittle Fracture: Formulation and Analysis Within the Isogeometric Analysis Framework," *Computer Methods in Applied Mechanics and Engineering* 273 (2014): 100–118.

12. J.-Y. Wu, “A Unified Phase-Field Theory for the Mechanics of Damage and Quasi-Brittle Failure,” *Journal of the Mechanics and Physics of Solids* 103 (2017): 72–99.

13. T.-T. Nguyen, J. Yvonnet, D. Waldmann, and Q.-C. He, “Implementation of a New Strain Split to Model Unilateral Contact Within the Phase Field Method,” *International Journal for Numerical Methods in Engineering* 121, no. 21 (2020): 4717–4733.

14. R. Alessi, J.-J. Marigo, and S. Vidoli, “Gradient Damage Models Coupled With Plasticity: Variational Formulation and Main Properties,” *Mechanics of Materials* 80 (2015): 351–367.

15. A. Karma, D. A. Kessler, and H. Levine, “Phase-Field Model of Mode Iii Dynamic Fracture,” *Physical Review Letters* 87, no. 4 (2001): 045501.

16. C. Kuhn and R. Müller, “A Phase Field Model for Fracture,” in *PAMM: Proceedings in Applied Mathematics and Mechanics*, vol. 8 (Wiley Online Library, 2008), 10223–10224.

17. E. Lorentz, S. Cuvilliez, and K. Kazymyrenko, “Modelling Large Crack Propagation: From Gradient Damage to Cohesive Zone Models,” *International Journal of Fracture* 178, no. 1 (2012): 85–95.

18. C. Steinke and M. Kaliske, “A Phase-Field Crack Model Based on Directional Stress Decomposition,” *Computational Mechanics* 63 (2019): 1019–1046.

19. J.-Y. Wu, V. P. Nguyen, H. Zhou, and Y. Huang, “A Variationally Consistent Phase-Field Anisotropic Damage Model for Fracture,” *Computer Methods in Applied Mechanics and Engineering* 358 (2020): 112629.

20. S. Zhang, W. Jiang, and M. R. Tonks, “A New Phase Field Fracture Model for Brittle Materials That Accounts for Elastic Anisotropy,” *Computer Methods in Applied Mechanics and Engineering* 358 (2020): 112643.

21. V. Ziaei-Rad, M. Mollaali, T. Nagel, O. Kolditz, and K. Yoshioka, “Orthogonal Decomposition of Anisotropic Constitutive Models for the Phase Field Approach to Fracture,” *Journal of the Mechanics and Physics of Solids* 171 (2023): 105143.

22. C. Bilgen, A. Kopaničáková, R. Krause, and K. Weinberg, “A Phase-Field Approach to Pneumatic Fracture,” in *Non-Standard Discretisation Methods in Solid Mechanics* (Springer, 2022), 217–241.

23. J. Bleyer and R. Alessi, “Phase-Field Modeling of Anisotropic Brittle Fracture Including Several Damage Mechanisms,” *Computer Methods in Applied Mechanics and Engineering* 336 (2018): 213–236.

24. J. Clayton and J. Knap, “Phase Field Modeling of Directional Fracture in Anisotropic Polycrystals,” *Computational Materials Science* 98 (2015): 158–169.

25. F. Fei and J. Choo, “Double-Phase-Field Formulation for Mixed-Mode Fracture in Rocks,” *Computer Methods in Applied Mechanics and Engineering* 376 (2021): 113655.

26. T. Gerasimov and L. De Lorenzis, “Second-Order Phase-Field Formulations for Anisotropic Brittle Fracture,” *Computer Methods in Applied Mechanics and Engineering* 389 (2022): 114403.

27. B. Li and C. Maurini, “Crack Kinking in a Variational Phase-Field Model of Brittle Fracture With Strongly Anisotropic Surface Energy,” *Journal of the Mechanics and Physics of Solids* 125 (2019): 502–522.

28. B. Li, C. Peco, D. Millán, I. Arias, and M. Arroyo, “Phase-Field Modeling and Simulation of Fracture in Brittle Materials With Strongly Anisotropic Surface Energy,” *International Journal for Numerical Methods in Engineering* 102, no. 3–4 (2015): 711–727.

29. T.-T. Nguyen, J. Réthoré, J. Yvonnet, and M.-C. Baietto, “Multi-Phase-Field Modeling of Anisotropic Crack Propagation for Polycrystalline Materials,” *Computational Mechanics* 60 (2017): 289–314.

30. N. Noii, F. Aldakheel, T. Wick, and P. Wriggers, “An Adaptive Global–Local Approach for Phase-Field Modeling of Anisotropic Brittle Fracture,” *Computer Methods in Applied Mechanics and Engineering* 361 (2020): 112744.

31. J.-M. Scherer, S. Brach, and J. Bleyer, “An Assessment of Anisotropic Phase-Field Models of Brittle Fracture,” *Computer Methods in Applied Mechanics and Engineering* 395 (2022): 115036.

32. S. Teichtmeister, D. Kienle, F. Aldakheel, and M.-A. Keip, “Phase Field Modeling of Fracture in Anisotropic Brittle Solids,” *International Journal of Non-Linear Mechanics* 97 (2017): 1–21.

33. M. Ambati, T. Gerasimov, and L. De Lorenzis, “Phase-Field Modeling of Ductile Fracture,” *Computational Mechanics* 55 (2015): 1017–1040.

34. J. Bleyer, C. Roux-Langlois, and J.-F. Molinari, “Dynamic Crack Propagation With a Variational Phase-Field Model: Limiting Speed, Crack Branching and Velocity-Toughening Mechanisms,” *International Journal of Fracture* 204, no. 1 (2017): 79–100.

35. M. J. Borden, C. V. Verhoosel, M. A. Scott, T. J. Hughes, and C. M. Landis, “A Phase-Field Description of Dynamic Brittle Fracture,” *Computer Methods in Applied Mechanics and Engineering* 217 (2012): 77–95.

36. L. Chen and R. de Borst, “Phase-Field Modelling of Cohesive Fracture,” *European Journal of Mechanics–A/Solids* 90 (2021): 104343.

37. P. Li, J. Yvonnet, and C. Combescure, “An Extension of the Phase Field Method to Model Interactions Between Interfacial Damage and Brittle Fracture in Elastoplastic Composites,” *International Journal of Mechanical Sciences* 179 (2020): 105633.

38. L. Xia, J. Yvonnet, and S. Ghabezloo, “Phase Field Modeling of Hydraulic Fracturing With Interfacial Damage in Highly Heterogeneous Fluid-Saturated Porous Media,” *Engineering Fracture Mechanics* 186 (2017): 158–180.

39. P. Li, Y. Wu, and J. Yvonnet, “A Simp-Phase Field Topology Optimization Framework to Maximize Quasi-Brittle Fracture Resistance of 2d and 3d Composites,” *Theoretical and Applied Fracture Mechanics* 114 (2021): 102919.

40. T. T. Nguyen, J. Yvonnet, M. Bornert, and C. Chateau, “Initiation and Propagation of Complex 3d Networks of Cracks in Heterogeneous Quasi-Brittle Materials: Direct Comparison Between In Situ Testing-Microct Experiments and Phase Field Simulations,” *Journal of the Mechanics and Physics of Solids* 95 (2016): 320–350.

41. T. T. Nguyen, J. Yvonnet, M. Bornert, C. Chateau, F. Bilteryst, and E. Steib, “Large-Scale Simulations of Quasi-Brittle Microcracking in Realistic Highly Heterogeneous Microstructures Obtained From Micro Ct Imaging,” *Extreme Mechanics Letters* 17 (2017): 50–55.

42. T. T. Nguyen, J. Yvonnet, Q.-Z. Zhu, M. Bornert, and C. Chateau, “A Phase Field Method to Simulate Crack Nucleation and Propagation in Strongly Heterogeneous Materials From Direct Imaging of Their Microstructure,” *Engineering Fracture Mechanics* 139 (2015): 18–39.

43. R. Bharali, S. Goswami, C. Anitescu, and T. Rabczuk, “A Robust Monolithic Solver for Phase-Field Fracture Integrated With Fracture Energy Based Arc-Length Method and Under-Relaxation,” *Computer Methods in Applied Mechanics and Engineering* 394 (2022): 114927.

44. T. Gerasimov and L. De Lorenzis, “A Line Search Assisted Monolithic Approach for Phase-Field Computing of Brittle Fracture,” *Computer Methods in Applied Mechanics and Engineering* 312 (2016): 276–303.

45. C. Gräser, D. Kienle, and O. Sander, “Truncated Nonsmooth Newton Multigrid for Phase-Field Brittle-Fracture Problems, With Analysis,” *Computational Mechanics* 72, no. 5 (2023): 1059–1089, https://doi.org/10.1007/s00466-023-02330-x.

46. T. Wick, “Modified Newton Methods for Solving Fully Monolithic Phase-Field Quasi-Static Brittle Fracture Propagation,” *Computer Methods in Applied Mechanics and Engineering* 325 (2017): 577–611.

47. J.-Y. Wu, Y. Huang, and V. P. Nguyen, “On the BFGS Monolithic Algorithm for the Unified Phase Field Damage Theory,” *Computer Methods in Applied Mechanics and Engineering* 360 (2020): 112704.

48. P. Farrell and C. Maurini, “Linear and Nonlinear Solvers for Variational Phase-Field Models of Brittle Fracture,” *International Journal for Numerical Methods in Engineering* 109, no. 5 (2017): 648–667.

49. Message Passing Interface Forum, “MPI: A Message-Passing Interface Standard Version 4.1,” 2023.

50. “OpenMP Application Programming Interface,” 2023 OpenMP Technical Report 12:Version 6.0 Preview 2.

51. NVIDIA, P. Vingelmann, and F. H. Fitzek, “Cuda, Release: 10.2.89,” 2020, https://developer.nvidia.com/cuda-toolkit.

52. C. Farhat, M. Lesoinne, and K. Pierson, “A Scalable Dual-Primal Domain Decomposition Method,” *Numerical Linear Algebra With Applications* 7, no. 7–8 (2000): 687–714.

53. C. Farhat and F.-X. Roux, “The Dual Schur Complement Method,” in *Domain Decomposition Methods in Science and Engineering: The Sixth International Conference on Domain Decomposition*, vol. 157 (American Mathematical Society, 1994).

54. C. Farhat, M. Lesoinne, P. LeTallec, K. Pierson, and D. Rixen, “Feti-Dp: A Dual–Primal Unified Feti Method—Part i: A Faster Alternative to the Two-Level Feti Method,” *International Journal for Numerical Methods in Engineering* 50, no. 7 (2001): 1523–1544.

55. C. Farhat and F.-X. Roux, “A Method of Finite Element Tearing and Interconnecting and Its Parallel Solution Algorithm,” *International Journal for Numerical Methods in Engineering* 32, no. 6 (1991): 1205–1227.

56. J. Mandel, “Balancing Domain Decomposition,” *Communications in Numerical Methods in Engineering* 9, no. 3 (1993): 233–241.

57. M. Heinkenschloss and H. Nguyen, “Neumann–Neumann Domain Decomposition Preconditioners for Linear-Quadratic Elliptic Optimal Control Problems,” *SIAM Journal on Scientific Computing* 28, no. 3 (2006): 1001–1028.

58. P. Le Tallec, J. Mandel, and M. Vidrascu, “A Neumann–Neumann Domain Decomposition Algorithm for Solving Plate and Shell Problems,” *SIAM Journal on Numerical Analysis* 35, no. 2 (1998): 836–867.

59. M. Dryja and O. B. Widlund, *Additive Schwarz Methods for Elliptic Finite Element Problems in Three Dimensions* (Courant Institute of Mathematical Sciences, 1991).

60. L. F. Pavarino, “Additive Schwarz Methods for the p-Version Finite Element Method,” *Numerische Mathematik* 66, no. 1 (1993): 493–515, https://doi.org/10.1007/BF01385709.

61. T. A. Davis, “Algorithm 832: Umfpack v4. 3—An Unsymmetric-Pattern Multifrontal Method,” *ACM Transactions on Mathematical Software* 30, no. 2 (2004): 196–199.

62. J. W. Demmel, J. R. Gilbert, and X. S. Li, “Superlu Users’ Guide,” 1999.

63. P. R. Amestoy, A. Buttari, J.-Y. L’excellent, and T. Mary, “Performance and Scalability of the Block Low-Rank Multifrontal Factorization on Multicore Architectures,” *ACM Transactions on Mathematical Software* 45, no. 1 (2019): 1–26.

64. P. R. Amestoy, I. S. Duff, J.-Y. L’Excellent, and J. Koster, “A Fully Asynchronous Multifrontal Solver Using Distributed Dynamic Scheduling,” *SIAM Journal on Matrix Analysis and Applications* 23, no. 1 (2001): 15–41.

65. S. El Ouafa, S. Vincent, V. Le Chenadec, and B. Trouette, “Fully-Coupled Parallel Solver for the Simulation of Two-Phase Incompressible Flows,” *Computers & Fluids* 265 (2023): 105995.

66. Y. Saad and M. H. Schultz, “Gmres: A Generalized Minimal Residual Algorithm for Solving Nonsymmetric Linear Systems,” *SIAM Journal on Scientific and Statistical Computing* 7, no. 3 (1986): 856–869.

67. E. Stiefel, “Methods of Conjugate Gradients for Solving Linear Systems,” *Journal of Research of the National Bureau of Standards* 49, no. 6 (1952): 409–435, https://doi.org/10.6028/jres.049.044.

68. H. A. Van der Vorst, “Bi-Cgstab: A Fast and Smoothly Converging Variant of bi-Cg for the Solution of Nonsymmetric Linear Systems,” *SIAM Journal on Scientific and Statistical Computing* 13, no. 2 (1992): 631–644.

69. M. Benzi, G. H. Golub, and J. Liesen, “Numerical Solution of Saddle Point Problems,” *Acta Numerica* 14 (2005): 1–137.

70. D. Chen, “A Symmetric Successive Overrelaxation (Ssor) Based Gauss-Seidel Massive Mimo Detection Algorithm,” in *Journal of Physics: Conference Series*, vol. 1438 (IOP Publishing, 2020).

71. F. D. Mohammed and M. Rivaie, “Jacobi-Davidson, Gauss-Seidel and Successive Over-Relaxation for Solving Systems of Linear Equations,” *Applied Mathematics and Computational Intelligence (AMCI)* 6 (2017): 41–52.

72. Y. Notay, “An Aggregation-Based Algebraic Multigrid Method,” *Electronic Transactions on Numerical Analysis* 37 (2010): 123–146.

73. M. Rozložník, *Saddle-Point Problems and Their Iterative Solution* (Springer, 2018).

74. J. W. Ruge and K. Stüben, “Algebraic Multigrid,” in *Multigrid Methods* (SIAM, 1987), 73–130.

75. P. Vanek, J. Mandel, and M. Brezina, “Algebraic Multigrid by Smoothed Aggregation for Second and Fourth Order Elliptic Problems,” *Computing* 56, no. 3 (1996): 179–196.

76. S. Hao and Y. Shen, “An Efficient Parallel Solution Scheme for the Phase Field Approach to Dynamic Fracture Based on a Domain Decomposition Method,” *International Journal for Numerical Methods in Engineering* 125, no. 6 (2024): e7405.

77. D. Jodlbauer, U. Langer, and T. Wick, “Parallel Matrix-Free Higher-Order Finite Element Solvers for Phase-Field Fracture Problems,” *Mathematical and Computational Applications* 25, no. 3 (2020): 40.

78. X. Liu, J. Réthoré, and A. A. Lubrecht, “An Efficient Matrix-Free Preconditioned Conjugate Gradient Based Multigrid Method for Phase Field Modeling of Fracture in Heterogeneous Materials From 3d Images,” *Computer Methods in Applied Mechanics and Engineering* 388 (2022): 114266.

79. J. Rannou and C. Bovet, “Domain Decomposition Methods and Acceleration Techniques for the Phase Field Fracture Staggered Solver,” *International Journal for Numerical Methods in Engineering* 125, no. 7 (2023): e7544.

80. V. Ziaei-Rad and Y. Shen, “Massive Parallelization of the Phase Field Formulation for Crack Propagation With Time Adaptivity,” *Computer Methods in Applied Mechanics and Engineering* 312 (2016): 224–253.

81. M. Artina, M. Fornasier, S. Micheletti, and S. Perotto, “Anisotropic Mesh Adaptation for Crack Detection in Brittle Materials,” *SIAM Journal on Scientific Computing* 37, no. 4 (2015): B633–B659.

82. R. Assaf, C. Birk, S. Natarajan, and H. Gravenkamp, “Three-Dimensional Phase-Field Modeling of Brittle Fracture Using an Adaptive Octree-Based Scaled Boundary Finite Element Approach,” *Computer Methods in Applied Mechanics and Engineering* 399 (2022): 115364.

83. H. Badnava, M. A. Msekh, E. Etemadi, and T. Rabczuk, “An h-Adaptive Thermo-Mechanical Phase Field Model for Fracture,” *Finite Elements in Analysis and Design* 138 (2018): 31–47.

84. S. Burke, C. Ortner, and E. Süli, “An Adaptive Finite Element Approximation of a Variational Model of Brittle Fracture,” *SIAM Journal on Numerical Analysis* 48, no. 3 (2010): 980–1012.

85. T. Heister, M. F. Wheeler, and T. Wick, “A Primal-Dual Active Set Method and Predictor-Corrector Mesh Adaptivity for Computing Fracture Propagation Using a Phase-Field Approach,” *Computer Methods in Applied Mechanics and Engineering* 290 (2015): 466–495.

86. H. Hirshikesh, A. Pramod, H. Waisman, and S. Natarajan, “Adaptive Phase Field Method Using Novel Physics Based Refinement Criteria,” *Computer Methods in Applied Mechanics and Engineering* 383 (2021): 113874.

87. C. Jansari, K. Kannan, R. Annabattula, and S. Natarajan, “Adaptive Phase Field Method for Quasi-Static Brittle Fracture Using a Recovery Based Error Indicator and Quadtree Decomposition,” *Engineering Fracture Mechanics* 220 (2019): 106599.

88. R. Patil, B. Mishra, and I. Singh, “An Adaptive Multiscale Phase Field Method for Brittle Fracture,” *Computer Methods in Applied Mechanics and Engineering* 329 (2018): 254–288.

89. A. Pramod, R. Annabattula, E. Ooi, et al., “Adaptive Phase-Field Modeling of Brittle Fracture Using the Scaled Boundary Finite Element Method,” *Computer Methods in Applied Mechanics and Engineering* 355 (2019): 284–307.

90. T. Wick, “Goal Functional Evaluations for Phase-Field Fracture Using Pu-Based Dwr Mesh Adaptivity,” *Computational Mechanics* 57, no. 6 (2016): 1017–1035.

91. H. B. Dhia, “Multiscale Mechanical Problems: The Arlequin Method,” *Comptes Rendus de L’academie Des Sciences Series IIB Mechanics Physics Astronomy* 326, no. 12 (1998): 899–904.

92. H. B. Dhia and G. Rateau, “The Arlequin Method as a Flexible Engineering Design Tool,” *International Journal for Numerical Methods in Engineering* 62, no. 11 (2005): 1442–1462.

93. P.-A. Guidault and T. Belytschko, “On the l2 and the h1 Couplings for an Overlapping Domain Decomposition Method Using Lagrange Multipliers,” *International Journal for Numerical Methods in Engineering* 70, no. 3 (2007): 322–350.

94. S. Xiao and T. Belytschko, “A Bridging Domain Method for Coupling Continua With Molecular Dynamics,” *Computer Methods in Applied Mechanics and Engineering* 193, no. 17–20 (2004): 1645–1669.

95. T. Gerasimov, N. Noii, O. Allix, and L. De Lorenzis, “A Non-Intrusive Global/Local Approach Applied to Phase-Field Modeling of Brittle Fracture,” *Advanced Modeling and Simulation in Engineering Sciences* 5 (2018): 1–30.

96. L. Gendre, O. Allix, P. Gosselet, and F. Comte, “Non-Intrusive and Exact Global/Local Techniques for Structural Problems With Local Plasticity,” *Computational Mechanics* 44 (2009): 233–245.

97. P. Gupta, J. Pereira, D.-J. Kim, C. Duarte, and T. Eason, “Analysis of Three-Dimensional Fracture Mechanics Problems: A Non-Intrusive Approach Using a Generalized Finite Element Method,” *Engineering Fracture Mechanics* 90 (2012): 41–64.

98. M. Jaque-Zurita, J. Hinojosa, and I. Fuenzalida-Henríquez, “Global–Local Non Intrusive Analysis With 1d to 3d Coupling: Application to Crack Propagation and Extension to Commercial Software,” *Mathematics* 11, no. 11 (2023): 2540.

99. C. Oliver-Leblond, A. Delaplace, F. Ragueneau, and B. Richard, “Non-Intrusive Global/Local Analysis for the Study of Fine Cracking,” *International Journal for Numerical and Analytical Methods in Geomechanics* 37, no. 8 (2013): 973–992.

100. F. Aldakheel, N. Noii, T. Wick, O. Allix, and P. Wriggers, “Multilevel Global–Local Techniques for Adaptive Ductile Phase-Field Fracture,” *Computer Methods in Applied Mechanics and Engineering* 387 (2021): 114175.

101. F. Aldakheel, N. Noii, T. Wick, and P. Wriggers, “A Global–Local Approach for Hydraulic Phase-Field Fracture in Poroelastic Media,” *Computers & Mathematics with Applications* 91 (2021): 99–121.

102. P. Cheng, X. Zhuang, H. Zhu, and J. Fish, “Application of s-Version Finite Element Method to Phase Field Modeling for Localized Fractures,” *Computers and Geotechnics* 156 (2023): 105204.

103. D. Da, “Model Reduction on 3D Fracture Resistance Design,” *Journal of Computational Physics* 463 (2022): 111274.

104. N.-H. Nguyen, V. P. Nguyen, J.-Y. Wu, T.-H.-H. Le, and Y. Ding, “Mesh-Based and Meshfree Reduced Order Phase-Field Models for Brittle Fracture: One Dimensional Problems,” *Materials* 12, no. 11 (2019): 1858.

105. E. Storvik, J. W. Both, J. M. Sargado, J. M. Nordbotten, and F. A. Radu, “An Accelerated Staggered Scheme for Variational Phase-Field Models of Brittle Fracture,” *Computer Methods in Applied Mechanics and Engineering* 381 (2021): 113822.

106. C. Miehe and M. Lambrecht, “Algorithms for Computation of Stresses and Elasticity Moduli in Terms of Seth–Hill’s Family of Generalized Strain Tensors,” *Communications in Numerical Methods in Engineering* 17, no. 5 (2001): 337–353.

107. H. B. Dhia and G. Rateau, “Analyse mathématique de la méthode arlequin mixte,” *Comptes Rendus de L’académie Des Sciences-Series I-Mathematics* 332, no. 7 (2001): 649–654, https://doi.org/10.1016/S0764-4442(01)01900-0.

108. R. A. Adams and J. Fournier, *Sobolev Spaces*, vol. 19 (academic Press, 1975).

109. P. T. Bauman, H. B. Dhia, N. Elkhodja, J. T. Oden, and S. Prudhomme, “On the Application of the Arlequin Method to the Coupling of Particle and Continuum Models,” *Computational Mechanics* 42 (2008): 511–530.

110. H. Qiao, Q. Yang, W. Chen, and C. Zhang, “Implementation of the Arlequin Method Into Abaqus: Basic Formulations and Applications,” *Advances in Engineering Software* 42, no. 4 (2011): 197–207.

Appendix A

Coupling Matrices Computation

In this work, regular and compatible meshes are used (4-node quadrilateral elements). The integration of the discretized form of the coupling matrices is performed with the Gaussian quadrature using reference elements. The shape functions considered are expressed as:

$$N_1(\xi,\eta) = \frac{1}{4}(1-\xi)(1-\eta) \tag{A1}$$

$$N_2(\xi,\eta) = \frac{1}{4}(1+\xi)(1-\eta) \tag{A2}$$

$$N_3(\xi,\eta) = \frac{1}{4}(1+\xi)(1+\eta) \tag{A3}$$

$$N_4(\xi,\eta) = \frac{1}{4}(1-\xi)(1+\eta) \tag{A4}$$

The coupling matrix $\boldsymbol{C}_u^1$ in Equation (46) can be written as:

$$\begin{aligned}\boldsymbol{C}_u^1 = \int_{-1}^{1}\int_{-1}^{1}\Big[&\boldsymbol{N}_u^{1^T}(\xi_1,\eta_1)\boldsymbol{N}_u^1(\xi_1,\eta_1)\\ &+\ell_u^2\boldsymbol{B}_u^{1^T}(\xi_1,\eta_1)\boldsymbol{B}_u^1(\xi_1,\eta_1)\Big]J_1\,d\xi_1\,d\eta_1\end{aligned} \tag{A5}$$

where (ξ_1,η_1) are the reference coordinates and $\boldsymbol{J}_1$ is the Jacobian determinant associated with the coarse element (see Figure A1).

Using the Gaussian quadrature method, Equation (A5) yields to:

$$\begin{aligned}\boldsymbol{C}_u^1 = \sum_{GP=1}^{4}\Big[&\boldsymbol{N}_{uGP}^{1^T}(\xi_1^{GP},\eta_1^{GP})\boldsymbol{N}_{uGP}^1(\xi_1^{GP},\eta_1^{GP})\\ &+\ell_u^2\boldsymbol{B}_{uGP}^{1^T}(\xi_1^{GP},\eta_1^{GP})\boldsymbol{B}_{uGP}^1(\xi_1^{GP},\eta_1^{GP})\Big]J_1\omega_{GP}\end{aligned} \tag{A6}$$

where (ξ_1^{GP},η_1^{GP}) and ω_{GP} are the reference coordinates and the weights of the Gauss points GP associated with the coarse element, respectively.

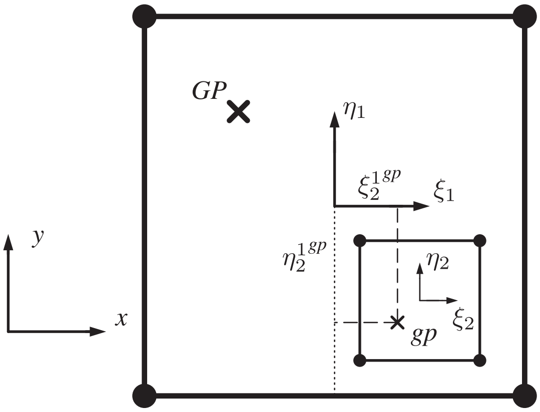

FIGURE A1 | Coarse and fine elements.

For the coupling matrix $\boldsymbol{C}_u^2$ in Equation (47), both coarse and fine elements are involved in the discretized form. Let us consider $\boldsymbol{u}^{gp}$ and $\boldsymbol{\varepsilon}^{gp}$ the displacement and strain vectors at the Gauss point gp (see Figure A1). Considering the fine element, $\boldsymbol{u}_{gp}$ and $\boldsymbol{\varepsilon}_{gp}$ are expressed as:

$$\boldsymbol{u}^{gp} = \boldsymbol{N}_u^2(\xi_2^{gp}, \eta_2^{gp})\boldsymbol{u}_2^i \tag{A7}$$

$$\boldsymbol{\varepsilon}^{gp} = \boldsymbol{B}_u^2(\xi_2^{gp}, \eta_2^{gp})\boldsymbol{u}_2^i \tag{A8}$$

where $\boldsymbol{u}_2^i$ are the nodal values of the displacement field $\boldsymbol{u}_2$ and $(\xi_2^{gp}, \eta_2^{gp})$ are the reference coordinates of the Gauss points gp in the fine element.

Considering the coarse element, $\boldsymbol{u}_{gp}$ and $\boldsymbol{\varepsilon}_{gp}$ are expressed as:

$$\boldsymbol{u}^{gp} = \boldsymbol{N}_u^1(\xi_2^{1gp}, \eta_2^{1gp})\boldsymbol{u}_1^i \tag{A9}$$

$$\boldsymbol{\varepsilon}^{gp} = \boldsymbol{B}_u^1(\xi_2^{1gp}, \eta_2^{1gp})\boldsymbol{u}_1^i \tag{A10}$$

where $\boldsymbol{u}_1^i$ are the nodal values of the displacement field $\boldsymbol{u}_1$ and $(\xi_2^{1gp}, \eta_2^{1gp})$ are the projection of the Gauss points of the fine element gp in the coarse element (see Figure A1).

Using Equations (A7–A10), the Equation (47) can be written as:

$$\begin{aligned}\boldsymbol{C}_u^2 = \int_{-1}^{1}\int_{-1}^{1} \Big[& \boldsymbol{N}_u^{1^T}(\xi_2^1, \eta_2^1)\boldsymbol{N}_u^2(\xi_2, \eta_2) \\ & + \ell_u^2 \boldsymbol{B}_u^{1^T}(\xi_2^1, \eta_2^1)\boldsymbol{B}_u^2(\xi_2, \eta_2)\Big] \boldsymbol{J}_2 d\xi_2 d\eta_2\end{aligned} \tag{A11}$$

where (ξ_2, η_2) and (ξ_2^1, η_2^1) are the reference coordinates in the fine element and their projections in the coarse element, respectively. $\boldsymbol{J}_2$ is the Jacobian determinant associated with the fine elements.

Using the Gaussian quadrature method, Equation (A11) yields:

$$\begin{aligned}\boldsymbol{C}_u^2 = \sum_{gp=1}^{4} \Big[& \boldsymbol{N}_{ugp}^{1^T}(\xi_2^{1gp}, \eta_2^{1gp})\boldsymbol{N}_{ugp}^2(\xi_2^{gp}, \eta_2^{gp}) \\ & + \ell_u^2 \boldsymbol{B}_{ugp}^{1^T}(\xi_2^{1gp}, \eta_2^{1gp})\boldsymbol{B}_{ugp}^2(\xi_2^{gp}, \eta_2^{gp})\Big] \boldsymbol{J}_2 \omega_{gp}\end{aligned} \tag{A12}$$

where $(\xi_2^{gp}, \eta_2^{gp})$ and ω_{gp} are the reference coordinates in the fine element and the weights of the Gauss points gp, respectively. $(\xi_2^{1gp}, \eta_2^{1gp})$ are the projection of the Gauss points gp in the coarse element.